Article

Current Biology

Functionally Distinct Gamma Range Activity Revealed by Stimulus Tuning in Human Visual Cortex

Graphical Abstract

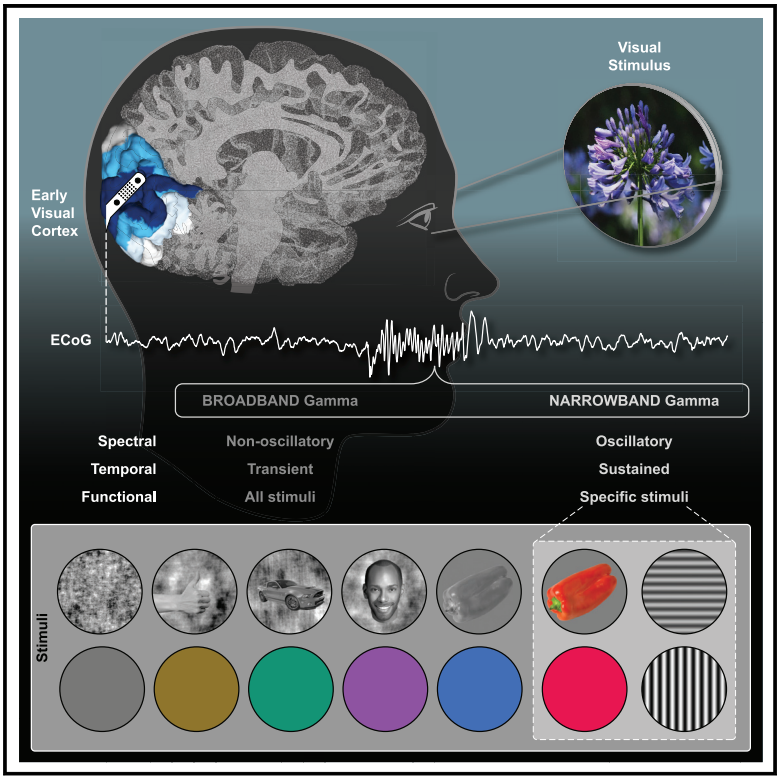

Authors

Eleonora Bartoli, William Bosking, Yvonne Chen, ..., Michael S. Beauchamp, Daniel Yoshor, Brett L. Foster

Correspondence

bfoster@bcm.edu

In Brief

Gamma oscillations are high-frequency neuro-electrical fluctuations (>20 Hz) proposed to support visual perception. Bartoli et al. use high-density intracranial recordings from the human visual cortex to reveal that gamma oscillations are only induced by specific structural and chromatic stimulus features, limiting their role in visual processing.

Highlights

- Temporal, spectral, and functional properties dissociate narrow and broadband gamma
- Narrowband gamma is tuned to visual gratings and long-wavelength hues (red/orange)
- Narrowband gamma responses to natural images reflect low-level stimulus tuning
- Stimulus dependencies limit the functional role of narrowband gamma oscillations

Bartoli et al., 2019, Current Biology 29, 3345–3358
October 21, 2019
https://doi.org/10.1016/j.cub.2019.08.004

CellPress

Current Biology
Article

CellPress

Functionally Distinct Gamma Range Activity Revealed by Stimulus Tuning in Human Visual Cortex

Eleonora Bartoli,[1] William Bosking,[1] Yvonne Chen,[1] Ye Li,[2] Sameer A. Sheth,[1,2] Michael S. Beauchamp,[1,2] Daniel Yoshor,[1,2] and Brett L. Foster[1,2,3,*]
[1]Department of Neurosurgery, Baylor College of Medicine, 1 Baylor Plaza, Houston, TX 77030, USA
[2]Department of Neuroscience, Baylor College of Medicine, 1 Baylor Plaza, Houston, TX 77030, USA
[3]Lead Contact
*Correspondence: bfoster@bcm.edu
https://doi.org/10.1016/j.cub.2019.08.004

SUMMARY

Neocortical gamma activity has long been hypothesized as a mechanism for synchronizing brain regions to support visual perception and cognition more broadly. Although early studies focused on narrowband gamma oscillations (~20–60 Hz), recent work has emphasized a more broadband "high-gamma" response (~70–150+ Hz). These responses are often conceptually or analytically treated as synonymous markers of gamma activity. Using high-density intracranial recordings from the human visual cortex, we challenge this view by showing distinct spectral, temporal, and functional properties of narrow and broadband gamma. Across four experiments, narrowband gamma was strongly selective for gratings and long-wavelength colors, displaying a delayed response onset, sustained temporal profile, and contrast-dependent peak frequency. In addition, induced narrowband gamma oscillations lacked phase consistency across stimulus repetitions and displayed highly focal inter-site synchronization. In contrast, broadband gamma was consistently observed for all presented stimuli, displaying a rapid response onset, transient temporal profile, and invariant spectral properties. We exploited stimulus tuning to highlight the functional dissociation of these distinct signals, reconciling prior inconsistencies across species and stimuli regarding the ubiquity of visual gamma oscillations during natural vision. The occurrence of visual narrowband gamma oscillations, unlike broadband high gamma, appears contingent on specific structural and chromatic stimulus attributes intersecting with the receptive field. Together, these findings have important implications for the study, analysis, and functional interpretation of neocortical gamma-range activity.

INTRODUCTION

Neocortical gamma oscillations, rhythmic neural population activity in the ~20- to 60-Hz frequency range, have historically been implicated in visual perception and cognitive processing more generally [1–4]. Early theoretical accounts posited that the synchronization of gamma oscillations within visual cortex supported the binding of disparate visual features [3–5]. This view has since been extended to propose the synchronization of gamma oscillations as a more general mechanism for inter-areal communication in neocortex, supporting higher cognitive function [2]. Central to these theories is the capacity for gamma oscillations to provide rhythmic control over spiking activity, allowing temporally coincident spiking between synchronized neocortical areas [6–8].

After early studies identifying neocortical gamma oscillations in the cat and non-human primate [9–11], investigations of the human brain sought to identify similar gamma-range activity patterns. Although early non-invasive methods, such as electro- and magneto-encephalography, provided evidence of neocortical gamma oscillations [12, 13], the >30-Hz frequency range presented challenges in dissociating small-amplitude, high-frequency activity from biological noise occupying a similar frequency range [14, 15]. Subsequent work using human intracranial recordings, which have superior sensitivity to high-frequency activity, suggested clear evidence of gamma-range responses [16]. However, in contrast to earlier animal work, these human studies most reliably identified activity in a higher and broader frequency range (e.g., spanning from 70 up to 150–200 Hz), leading many to describe these response patterns as "high gamma" [16]. Importantly, this high-gamma-range activity has been repeatedly observed across neocortical regions beyond visual cortex and is now commonly used as an indicator of local electrocortical response [17].

Despite these apparent spectral differences in what we will operationally term narrowband gamma (NBG) (i.e., gamma oscillations) and broadband gamma (BBG) (i.e., high gamma), these two signals are often conceptually and analytically conflated. However, growing evidence suggests these spectrally distinct responses are also temporally dissociated, owing to different biophysical generators [18]. Whereas NBG appears oscillatory, reflecting synchronization in the local field potential (LFP), BBG is often observed as non-oscillatory, potentially reflecting local population spiking and other activities coincident with multi-unit activity (MUA) [18–20]. NBG and BBG may also be functionally dissociated, as growing evidence suggests NBG, unlike BBG, is highly stimulus dependent in at least two ways. First, properties such as the amplitude and frequency of NBG are dependent on stimulus attributes (e.g., stimulus size

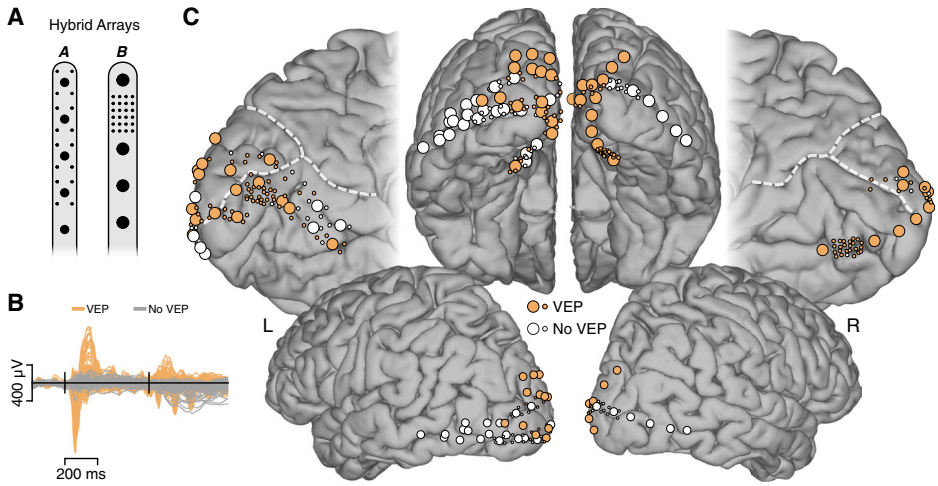

Figure 1. Electrode Arrays and Visually Responsive Recording Sites

(A) Schematic of hybrid macro- and mini-ECoG electrode arrays employed. Standard clinical strip arrays with macro-electrodes were customized to include small diameter mini-electrodes in two configurations. Macro-electrodes had diameters of 2 mm (array A; subjects N1–5) and 3 mm (array B; subjects N6–10), with mini-electrodes having a diameter of 0.5 mm (both arrays).

(B) To functionally select visually responsive electrodes, we used the visual evoked potential (VEP). Mean voltage traces are shown for VEP (orange) and non-VEP (gray) electrodes. Black vertical lines indicate stimulus onset and offset. From a total of 205 electrodes shown, 133 (~65%) displayed a VEP (data from subjects N1–7).

(C) Anatomical location of electrodes from subjects participating in the visual grating task is shown on a standard cortical surface (see Figure S1 and Table S1 for single-subject locations; Figures S4 and S5 for task responses mapped onto locations). Electrodes displaying a VEP are shown in orange (non-VEP in white). Dashed white lines indicate the parieto-occipital and calcarine sulci.

or contrast) [21–24]. This parametric relationship between stimulus attributes and NBG modulation has also been clearly quantified with non-invasive methods (e.g., [25–28]). Second, the occurrence of NBG itself may be contingent on specific types of stimuli, showing a strong preference for commonly used visual gratings rather than complex or natural stimuli [29].

Gamma-range activity is readily used as a signature for sensory or cognitive processing in many areas of systems neuroscience [2]. Therefore, the issue of clearly dissociating NBG and BBG activities to elucidate their spectral, temporal, and functional differences is critical in adjudicating the genuine role these activities play in sensory and cognitive processing. However, sensitive measurement of these responses can be challenging using non-invasive techniques, and invasive studies have predominantly been performed in non-human primates, with some key exceptions [24, 29]. It is, therefore, important to integrate these findings across species by using similar experimental manipulations and comparable measurement resolution in larger study cohorts. To achieve this, we used high-density macro- and mini-electrocorticography (ECoG) recordings from human visual cortex during four visual experiments that aimed to induce, manipulate, and dissociate NBG and BBG. Overall, we observed a sustained amplitude increase within a narrow frequency range (i.e., NBG) to be induced reliably by grating stimuli, whose contrast level determined the peak frequency of the induced oscillation, and by long-wavelength colors (i.e., red/orange). This stimulus dependence was not observed at higher frequency ranges, which showed a broadband increase in amplitude without any characteristic spectral peak (i.e., BBG), occurring transiently at stimulus onset and offset and similarly across different visual stimuli. Our findings have clear import for the detection, interpretation, and functional role of neocortical gamma-range activity in vision and cognition more broadly.

RESULTS

Identification of Responsive Sites in Early Visual Cortex

In the current study, we used high-density ECoG recordings from human visual cortex in 10 subjects undergoing invasive monitoring for the surgical treatment of refractory epilepsy. Recordings were performed using hybrid electrodes arrays, where mini-ECoG electrodes (0.5 mm diameter) were fabricated in between standard macro-ECoG electrode (2 or 3 mm diameter) strip arrays in two configurations (Figures 1 and S1). We employed a functional criterion to identify responsive electrodes within early visual cortex based on the presence of a visual-evoked potential (VEP). The VEP served as a measure of visual responsiveness that is partially independent from NBG and BBG. Of all the electrodes anatomically localized to the occipital lobe, approximately 57% (170/298 electrodes, considering all subjects) displayed a VEP, with evoked components similar to those classically identified in scalp (e.g., N1 occurring around ~70 ms) and intracranial recordings [30]. Of the electrodes displaying a VEP, ~83% were within V1/V2 (142/170), ~16% within V3/V4 (27/170), and only 1 electrode outside of V1–V4 (see Table S1; STAR Methods for details).

Visual Grating Stimuli Induce NBG and BBG Responses

In Experiment 1, our first aim was to quantify gamma-range activity in early visual cortex in response to visual gratings. Subjects were presented with full-screen static grayscale grating

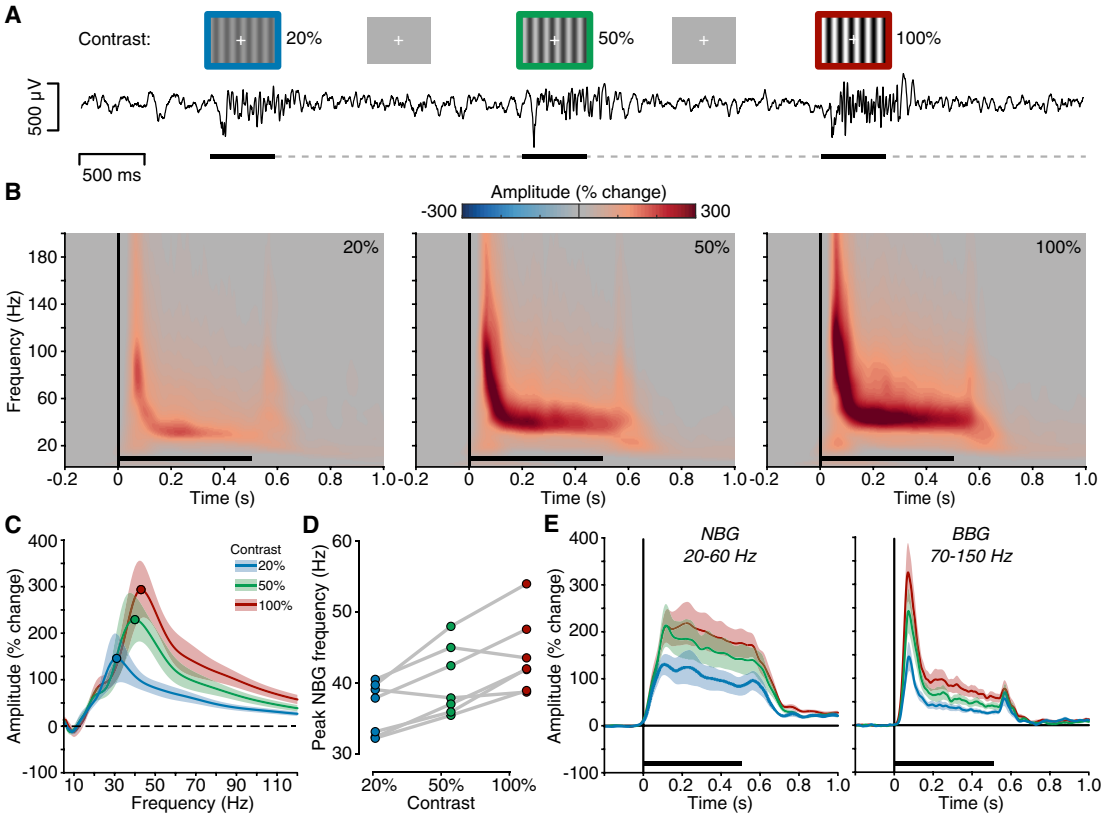

Figure 2. Experiment 1: Spectral Response to Visual Grating Stimuli

(A) Experiment 1 stimuli and example voltage response (from subject N6). Static grating stimuli were presented for 500 ms (black line), with a random inter-stimulus interval (ISI) (dashed line) of 1.5–2.0 s. Gratings were presented at 20%, 50%, and 100% contrast levels (represented in blue, green, and red, respectively).

(B) Group average spectrograms are shown for each grating contrast level; color maps reflect percentage change in amplitude relative to the pre-stimulus period (black line indicates stimulus presentation). See also Figures S2 and S3.

(C) Group average normalized amplitude spectra (percent change) for each contrast condition averaged from the 250- to 500-ms post-stimulus time window (filled circles indicate peak amplitude frequency; shading reflects SEM).

(D) Peak frequency of induced NBG for each subject across grating contrast levels (see Figures S4 and S5). Together, (B)–(D) clearly show a systematic increase in the NBG peak frequency with increasing contrast levels.

(E) Group mean amplitude time course for NBG and BBG ranges. Although NBG shows a more sustained temporal profile, BBG shows transient increases at stimulus onset and offset (shading reflects SEM).

stimuli (spatial frequency 1 cycle/degree) for 500 ms. Gratings were presented at three contrast levels (20%, 50%, and 100%). For many recordings, grating stimuli induced clear oscillatory responses in the raw ECoG voltage, identifiable on single trials (Figure 2A). Time-frequency analysis revealed these oscillatory responses to be induced NBG activity. Group-averaged time-frequency plots (Figure 2B) indicate that induced NBG shows a sustained increase in amplitude, within a frequency range (~20–60 Hz) consistent with prior human and non-human primate studies [31]. In addition, at stimulus onset and offset, transient amplitude increases were observed, which extend into a higher BBG (~70–150 Hz) range. These group spectrograms include both macro- and mini-ECoG electrodes, as both electrode types showed highly consistent responses and were therefore combined in subsequent analysis (Figures S2 and S7). Next, we examined how these gamma-range responses were influenced by changes in visual grating contrast.

NBG Oscillation Peak Frequency Is Related to Visual Grating Contrast

Previous work has suggested that changes in grating properties, such as contrast, influence the amplitude and frequency of NBG oscillations [21, 24, 27, 28]. Group-averaged time-frequency plots clearly show that increases in grating contrast induce both an increase in NBG amplitude and peak frequency (Figure 2B). These time-frequency plots include both presented orientations (0° and 90°), as they did not produce differing effects on NBG amplitude or frequency (Figure S2). To more accurately evaluate the influence of grating contrast on NBG activity, we averaged values in the time window between 250 and 500 ms post-stimulus onset, avoiding transient responses at stimulus onset and offset. However, we note that removal of VEP transients did not seriously impact group mean spectrogram properties of either NBG or BBG (Figures S3 and S4). Figure 2C shows the group mean normalized amplitude spectra for each

contrast condition. With increasing levels of contrast, the amplitude and peak frequency of NBG oscillations increased.

To obtain a more precise quantification of this effect and its variability, we identified NBG peak frequency at the single-trial level and then averaged across trials (separately for each contrast level) and across electrodes (separately for each participant). Specifically, grating contrast strongly influenced the NBG peak frequency, on average inducing a 4-Hz shift in the peak frequency for each contrast level increment (mean peak frequency and SE for 20% contrast: 36.4 ± 1.4 Hz; 50% contrast: 40.2 ± 1.9 Hz; 100% contrast: 43.8 ± 2.03 Hz; main contrast effect $F(2,12) = 14.62$, $p = 0.0006$; Figures 2D and S4B). Post hoc comparisons confirmed that NBG peak frequency was statistically different between each contrast level (all $p < 0.05$ Bonferroni corrected, from now p_{corr}). Peak amplitude was also significantly modulated by grating contrast, increasing on average from ~250% to 400% signal change from low to high contrast ($F(2,12) = 22.3$; $p < 0.0001$; all post hoc comparisons $p_{corr} < 0.05$; Figure S4C). In comparison, BBG, although increasing in amplitude across contrast levels (Figures 2B, 2C, and S4D), did not display any characteristic spectral changes.

Gratings Contrast Can Be Decoded Better Using NBG Than BBG

Given the strong influence of grating contrast level on induced peak frequency of NBG, we sought to test the reliability of this effect by decoding contrast levels using single-trial normalized amplitude spectra over the NBG range for each electrode. Using a support vector machine with cross validation, grating contrast could be decoded significantly above chance for each subject (chance = 0.33). Overall, 76% of visually responsive electrodes showed significant classification accuracy (101/133 VEP sites; considering subjects N1–N7). When using BBG as the feature, significant classification was achieved in only 35% of visually responsive electrodes (47/133). These data highlight a significantly greater number of electrodes that could successfully classify the stimulus contrast level using NBG versus BBG ($\chi^2(1) = 44.41$, $p < 0.001$; median accuracy NBG = 0.55, BBG = 0.39; Wilcoxon signed-rank test $p < 0.001$; Figure S5). To test the utility of our VEP selection of responsive sites, we also tested classification, including non-VEP occipital sites. These data displayed a similar trend, where 61% of electrodes (125/205) showed significant classification using NBG versus 25% using BBG (52/205). The anatomical distribution of classification accuracy closely matched the distribution of VEP sites (Figures S4 and S5). More generally, electrodes outside of the occipital lobe did not show any significant classification (Figure S5).

NBG and BBG Display Different Temporal Responses to Visual Gratings

A notable difference between NBG and BBG was the temporal profile of response (Figure 2B). Figure 2E shows the mean time course of NBG and BBG (after having averaged the normalized amplitude spectra within the 20–60 Hz and 70–150 Hz frequency ranges, respectively). NBG showed a sustained response throughout stimulus presentation, and the BBG response was transiently increased in amplitude at stimulus onset and offset. BBG did not return to baseline values between onset and offset, showing an additional sustained response, although of much smaller amplitude with respect to NBG (a temporal profile highly consistent with spiking activity under similar stimulus conditions) [21]. To quantify these temporal dynamics, we calculated the relative onset time of NBG and BBG activity at the single-trial level (STAR Methods for details and control analyses). On average, NBG had an onset latency of ~130 ms across conditions, and BBG onset occurred earlier, at ~80 ms (NBG onset: 131.7 ± 9.7 ms; BBG onset: 77.5 ± 14.5 ms; $t(6) = 4.9$; $p < 0.01$).

NBG Oscillations Display Variable Phase Clustering across Trials

To assess whether NBG oscillations displayed phase-locking during stimulus presentation, we computed a measure of phase consistency across trials (referred to throughout as inter-trial phase clustering [ITPC]) [32]. ITPC was calculated for the different contrast levels separately. As shown in Figure 3A, significant phase clustering was present at the onset and offset of stimuli, in a broadband range spanning from low to high frequencies (2–160 Hz; occurring between 0–200 ms and 500–700 ms post-stimulus; $p_{corr} < 0.05$; see also Figure S3). Interestingly, no reliable ITPC was found throughout stimulus presentation in the NBG range, during which NBG amplitudes are maximal. Thus, across-trial phase consistency was present only at stimulus onset and offset, with no consistent phase similarity being maintained during stimulus presentation. Although NBG phase dynamics may temporally vary across trials, these oscillations may still be phase consistent with other brain regions. Therefore, we next tested whether the phase relationship between electrodes would be consistent during stimulus presentation.

NBG Oscillations Display Local Phase Clustering between Sites

To test for evidence of phase consistency across visual cortex, we computed a measure of phase-based consistency (referred to throughout as inter-site phase clustering [ISPC]) [33] across all pairs of electrodes within each subject. ISPC was present at stimulus onset, in a broadband range spanning from low to high frequencies, similar to the ITPC pattern (5–120 Hz; occurring between 0 and 200 ms; $p_{corr} < 0.05$; Figure 3B). In addition, there was evidence of a weaker but significant ISPC in the NBG range, sustained throughout stimulus duration (between 30 and 60 Hz and occurring from ~100 to 500–600 ms post-stimulus).

We next exploited the high density of the electrode arrays used in this study to investigate the relation between phase consistency and inter-electrode distances. Figure 3C shows NBG ISPC for all electrode pairs (n = 1,252) as a function of electrode pair distance for the three contrast levels (NBG ISPC was averaged within a 250- to 500-ms time window and the 20- to 60-Hz frequency range, consistent with all analyses above). To quantify this relationship, we fitted an exponential decay function to the NBG ISPC over distance and obtained similar decay dynamics for the three contrast levels, with a spatial decay constant (distance needed to observe a 1/*e* drop of phase-consistency values, i.e., a 37% decrease) ranging from around 2.3 to 2.5 mm (Figure 3C; see Figure S6 for other phase-based synchrony measures). Consistent with previous work in non-human primates, these data suggest that induced NBG is synchronous locally for distances less than 5 mm [22]. To confirm that the rate

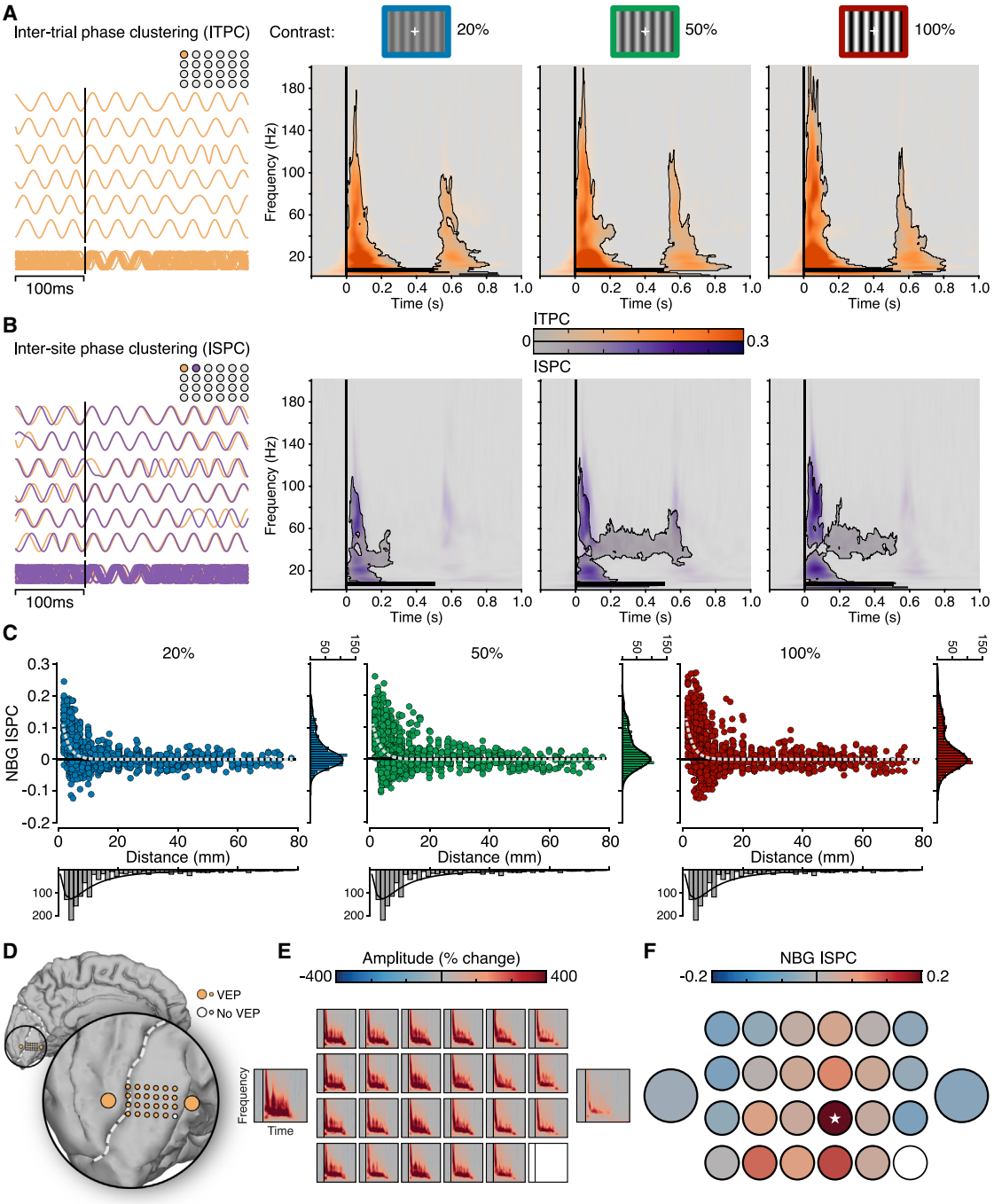

Figure 3. Inter-trial and Inter-site Phase Properties of NBG

(A) Time-frequency plots show group mean inter-trial phase clustering (ITPC) for each contrast condition. ITPC shows broadband clustering for stimulus onset and offset for each contrast level (contour lines indicate $p_{corr} < 0.05$; see also Figure S3). On the left, examples of NBG phase across repeated trials for an electrode, used for estimating ITPC, are shown.

(B) Time-frequency plots show group mean inter-site phase clustering (ISPC) for each contrast condition (based on all 1,252 electrode pairs; contour lines indicate $p_{corr} < 0.05$; see Figure S6). ISPC shows broadband clustering for stimulus onset followed by sustained NBG ISPC predominately for the 50% and 100% contrast levels. On the left, two example electrodes used for estimating ISPC are shown. ITPC and ISPC reflect normalized values relative to the pre-stimulus period.

(C) NBG ISPC is shown for each electrode pair as a function of inter-electrode distance for each contrast condition. Data are fitted with an exponential decay function (dashed line).

(D) Electrode location of macro- and mini-ECoG grid in subject N7.

(legend continued on next page)

of decay observed was reliably present also when considering single-subject data, we report an example of a mini-ECoG grid array in subject N7. The mini-ECoG array displayed clear NBG responses to visual gratings (Figures 3D and 3E), yet phase consistency was present only at neighboring electrodes (Figure 3F) within 2–6 mm.

Natural Image Stimuli Induce BBG, but Not Reliable NBG, Responses

It is currently debated whether NBG oscillations are consistently induced during the viewing of natural images, with evidence supporting both possibilities [34–37]. To test for the presence of NBG in response to natural images, in Experiment 2, we presented grayscale images of different visual categories (faces, houses, bodies, limbs, cars, words, numbers, and phase-scrambled noise) to a subset of our subjects (N3–N7). Images were presented for 1 s, and subjects were asked to perform an exemplar 1-back task responding to stimuli repeated back to back. The group mean spectrograms for each stimulus category show the clear presence of a BBG response at stimulus onset, spanning from ~20 to 200 Hz (Figure 4A). Strikingly, there is a lack of sustained NBG response to any of the visual categories presented with comparable spectral characteristics to Experiment 1. Otherwise, the responses recorded in early visual cortex were highly stereotyped across the different image categories, despite the diversity of image content. These observations were consistent for both macro- and mini-ECoG electrodes (Figure S7).

Next, we directly contrasted the spectral patterns in response to natural images versus gratings in subjects that performed both experiments (Figure 5). BBG responses were clearly visible in the power spectra for natural images, yet no peaks in the NBG range were observed. Conversely, NBG peaks were clearly visible on top of a broadband power increase for grating stimuli (Figure 5A). Similar spectral differences were also apparent when considering the non-normalized power spectra (Figure 5B), which also shows that the pre-stimulus baseline recordings were similar across experiments. To more precisely capture these task differences in the time-frequency domain, we constructed a ''task selectivity'' spectrogram (Figure 5C). For each recording site, we computed the difference in mean amplitude (% change) values between gratings (Experiment 1; all conditions) and natural images (Experiment 2; all conditions). The task selectivity spectrogram recapitulated the stimulus dependence described above for NBG and BBG, with gratings driving stronger NBG range responses and natural images driving stronger BBG responses. However, although this comparison helps to emphasize task differences, it is important to note that both experiments drove amplitude increases in NBG and BBG frequency ranges, but such increases reflect highly different response signatures (Figures 5A and 5B). Indeed, it is clear that the response to natural images is not confined to the frequency range >70 Hz but actually spans a broader range falling as low as 20 Hz. Figure 5D highlights this point by showing the group mean amplitude increases for NBG and BBG across all experimental conditions for early (0–250 ms) and late (250–500 ms) time windows. Critically, increases in NBG for grating stimuli are reflective of a spectral peak, whereas for natural images, it is simply part of a broadband amplitude increase extending into the NBG range.

For these reasons, caution must be taken when simply quantifying amplitude or power changes within this NBG range as synonymous with shifts in an oscillatory signal [38]. To deal with these issues of spectral overlap and genuine changes in NBG oscillations, we employed a further fitting procedure to automatically identify oscillatory peaks above the broadband aperiodic component in the power spectrum [38], similar to prior studies of NBG [29]. NBG oscillations, although prominent for the visual gratings, were not detected for natural images, as it was not possible to model the responses as containing one or more oscillations in the 20- to 150-Hz range (STAR Methods).

NBG Oscillations Display Color Selectivity

Unlike grating stimuli, we did not reliably observe NBG responses to natural image stimuli. However, one critical factor unaccounted for in our stimuli was image color. Indeed, recent observations in non-human primate V1 suggest that long-wavelength hues (red/orange) modulate visual NBG responses [39, 40]. Therefore, we next sought to test the potential for color stimuli to induce NBG oscillations using high-density ECoG recordings in human early visual cortex. Four subjects (N5 and N8–N10) performed Experiment 3, a visual color task, where they viewed full screen static colors (9 colors, including gray, equidistant in *CIE L*a*b** space) [41]. Importantly, color images contained no spatial structure or dynamic features to control for any edge or grating effects.

Responses to the visual color task are shown in Figure 6. Group mean spectrograms show BBG responses to be a somewhat common feature across colors—again being maximal at stimulus onset and offset. Most importantly, NBG responses are clearly visible for the red and orange colors only with similar spectral and temporal features as those observed for the visual grating task despite color stimuli lacking any grating-like spatial structure. This color tuning of NBG is more clearly seen in the group amplitude change spectra (Figure 6B). Amplitude change spectra showed that NBG responses (percent change from baseline in the 250- to 500-ms window) varied according to color from a maximal response to red/orange hues followed by blue/purple, green, and gray, as displayed in Figure 6C (non-parametric Friedman test of differences: $\chi^2(8) = 25.1$; $p < 0.01$). Although showing a lower but qualitatively similar pattern, the average BBG amplitude did not exhibit a reliable dependency on the hue value ($\chi^2(8) = 7.13$; $p = 0.52$). This weak though similar pattern in the BBG range may be partially accounted for by a secondary spectral peak, potentially reflecting a harmonic of the NBG signal. This feature is strikingly similar to observations

(E) Spectrograms show the mean amplitude response across the electrodes shown in (D) for the 100% contrast level.
(F) NBG ISPC for the same data in (D) and (E), relative to a seed electrode (indicated with a white star). Despite strong responses across electrodes, NBG ISPC is focal and rapidly decays within the mini-grid. The baseline-corrected ISPC values can range from −1 to 1 (with the seed being 1), but here, the color bar is clipped to smaller values (−0.2:0.2) to better capture the ISPC decay.

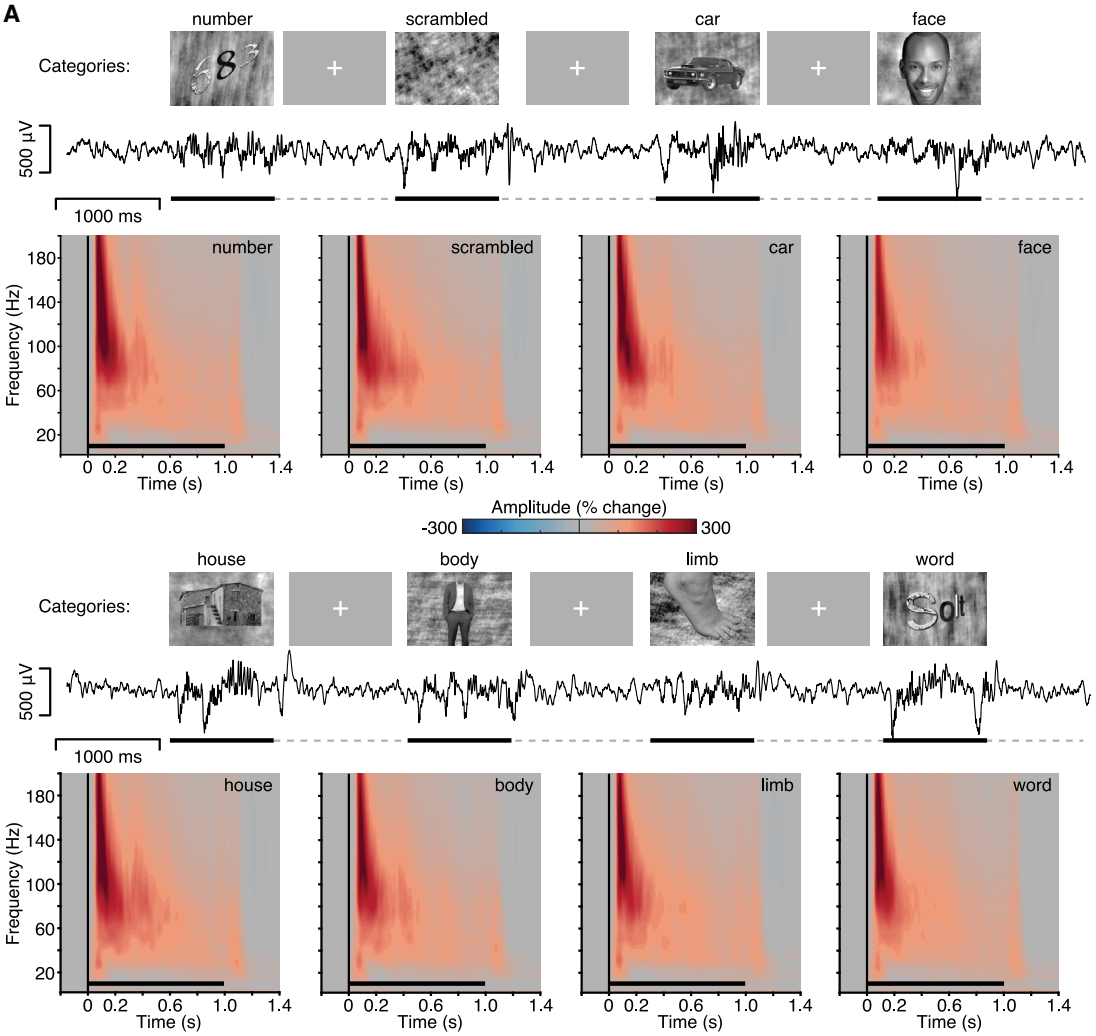

Figure 4. Experiment 2: Spectral Response to Natural Image Stimuli

Experiment 2 stimuli, example voltage response (subject N6; same as Figure 1A), and group mean spectrograms. Stimuli were grayscale images from eight visual categories (number, scramble, car, face, house, body, limb, and word), presented for 1,000 ms (black line), with a random ISI (dashed line) of 1–1.5 s (see also Figure S7). Mean group spectrograms show a highly consistent time-frequency response profile, typified by a strong BBG response to stimulus onset (color maps reflect percentage change in amplitude relative to the pre-stimulus period; black line indicates stimulus presentation).

reported in the non-human primate [39, 40]. Therefore, as commented above, caution must be used when considering power changes in a specific range without exploring the underlying spectral features. Although colors were selected from the same lightness plane ($L^* = 60$) in color space, differences in luminance could influence NBG responses across colors. To test this, we measured luminance values from the experimental monitor and found no correlation between luminance and NBG amplitude responses (STAR Methods).

Color and Grayscale Natural Images Induce Different Spectral Responses in the Gamma Range

Finally, in one subject (N10), we carried out Experiment 4 to explicitly test how color influences gamma-range responses to natural images. Among the electrodes displaying a VEP in the color task (Experiment 3), we selected those for which a robust receptive field could be identified (11 mini-ECoG electrodes; Figure 7A). Next, we analyzed the responses to the repeated presentation of a stimulus image both in grayscale and color (red bell pepper) positioned in the lower right visual field (so as to extend through the receptive field; Figure 7B). Mean spectrograms for the grayscale and color images display a clear enhancement of gamma-range activity for the colored image (Figure 7C). Interestingly, the response to this image is much larger in amplitude than those observed in Experiment 3 and is also higher in frequency. This higher frequency gamma peak (86 Hz) is more clearly seen for the amplitude change spectra (averaged over 250- to 500-ms window; Figure 7D). The single-trial amplitude spectra across repetitions of the grayscale and color image versions highlight the consistency of this gamma peak and the differences between conditions (Figure 7E).

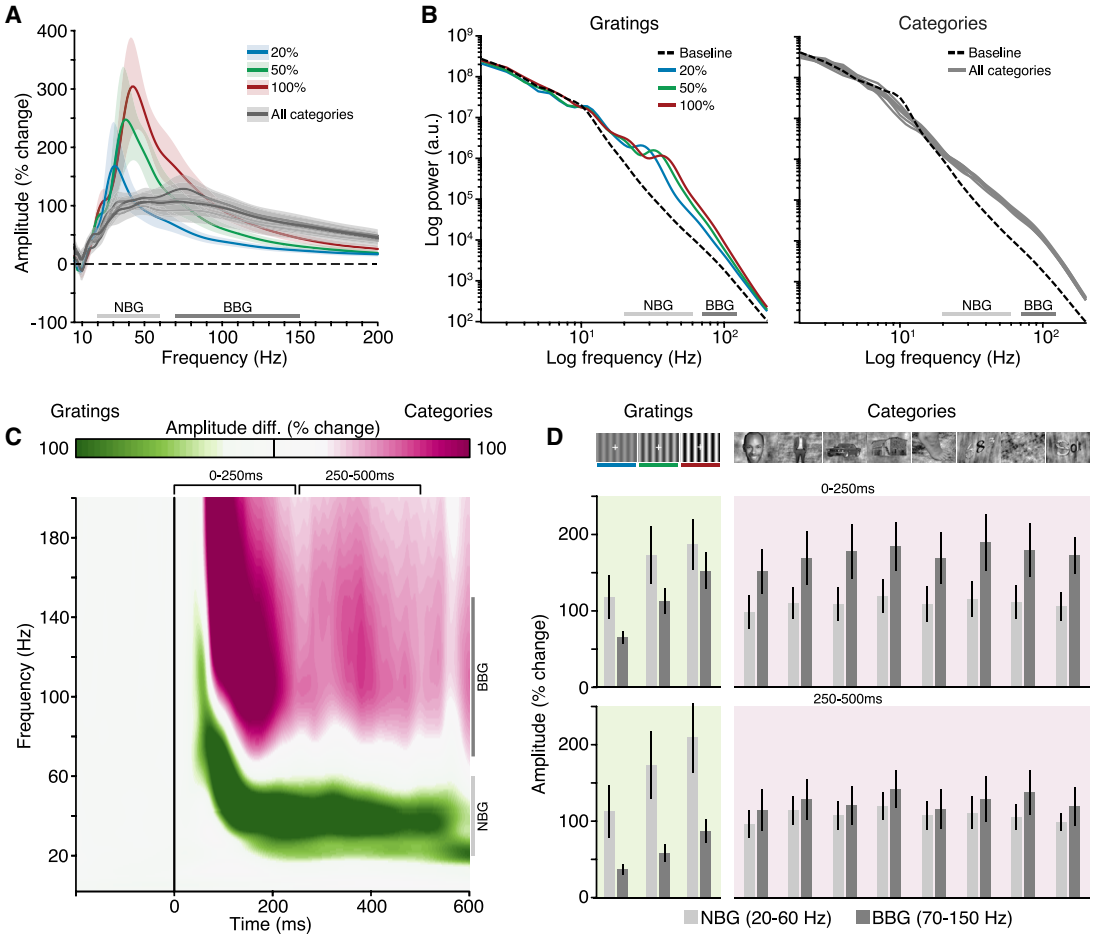

Figure 5. Experiments 1 and 2 Spectral Comparison

(A) Mean group normalized amplitude spectra (% change) are shown for all conditions across both experiments (image categories are given same gray color given highly overlapping data); shading reflects SEM.

(B) Mean group power spectra (log-log axis) are shown for both experiments, including mean baseline power spectra.

(C) Mean group "task selectivity" spectrogram (grating versus categories). Time-frequency map highlights amplitude of response relative to task (green for time-frequency points larger for gratings; purple for time-frequency points larger for categories; white for time-frequency points of similar amplitude across tasks). Conditions in both tasks have been collapsed (note: gratings are presented for 500 ms and natural images for 1,000 ms; map is truncated at 600 ms post-stimulus to capture stimulus presentation up until the offset response to gratings).

(D) Mean group amplitude response for NBG and BBG for early (0–250 ms) and late (250–500 ms) time windows (error bars, SEM). Across panels, NBG and BBG range is indicated for reference. Together, these plots highlight that BBG changes extend through the classical NBG range.

DISCUSSION

Using high-density intracranial recordings from early visual cortex in the human brain, we quantified distinct response properties of NBG and BBG to grating, natural image, and color stimuli. NBG and BBG reflect the historically defined gamma and high-gamma ranges, respectively.

For grating stimuli, NBG showed a sustained response throughout the stimulus duration, with a delayed onset (~130 ms). BBG showed a rapid (~80-ms) transient response to stimulus onset and offset. Across increasing levels of grating contrast, the peak frequency of NBG increased. BBG showed no reliable changes in frequency characteristics. Together, these response features supported successful classification of stimulus contrast, where classification accuracy was significantly greater for NBG. Across repetitions of grating trials, NBG displayed no consistent phase alignment. However, NBG did show phase consistency between nearby recording sites, which rapidly decayed with inter-electrode distance. Although broadband transients were seen for inter-trial and inter-site analysis, meaningful interpretation of BBG phase properties is problematic and potentially biased by event-related potentials. For grayscale natural images, no reliable NBG responses were observed, while robust BBG responses were present for all image categories. For color stimuli, NBG was most strongly induced by red/orange hues, with similar frequency and temporal characteristics as those observed for grating stimuli. Finally, we integrated these observations by showing how color tuning dramatically modulates the NBG response to natural images. Together, these findings clearly dissociate NBG and BBG

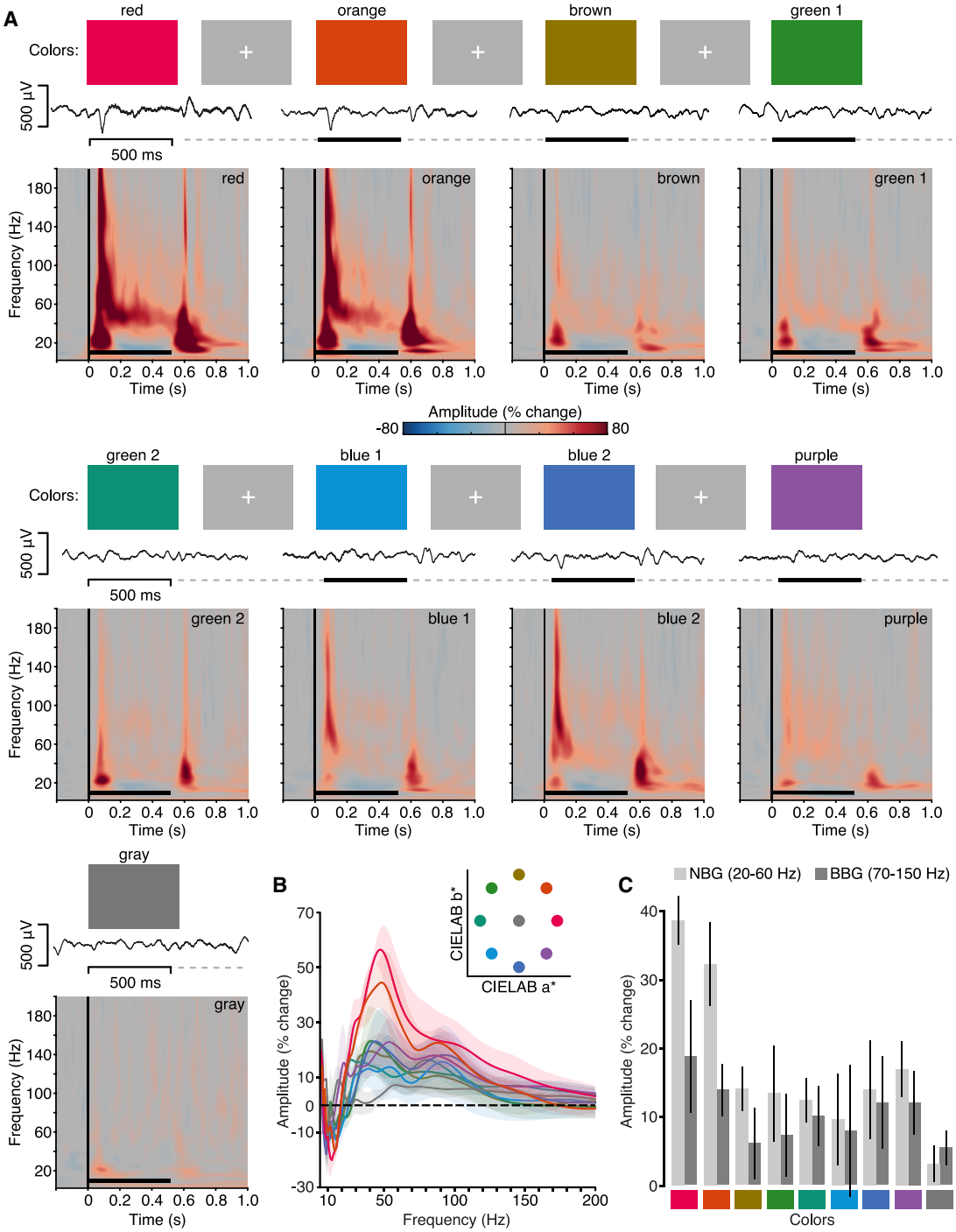

Figure 6. Experiment 3: Spectral Response to Color Stimuli

(A) Experiment 3 stimuli, example voltage response, and group mean spectrograms. Stimuli were full-screen colors from *CIE L*a*b** space (red, orange, yellow, green1, green2, blue1, blue2, purple, and gray), presented for 500 ms (black line), with a random ISI (dashed line) of 1.5–2 s. Example voltage response to stimuli is shown (subject N10). Mean group spectrograms show a variable time-frequency response profile depending on stimulus color, with a transient broadband response visible at onset and offset for most colors and a NBG response clearly visible for red/orange (color maps reflect percentage change in amplitude relative to the pre-stimulus period; black line indicates stimulus presentation).

(B) Group average normalized amplitude spectra (percent change) for each color averaged from the 250- to 500-ms post-stimulus time window (shading reflects SEM). Inset shows color stimuli location in CIE L*a*b* space (lightness plane L = 60).

(C) Mean group amplitude response across colors for NBG and BBG (250- to 500-ms time window; error bars, SEM).

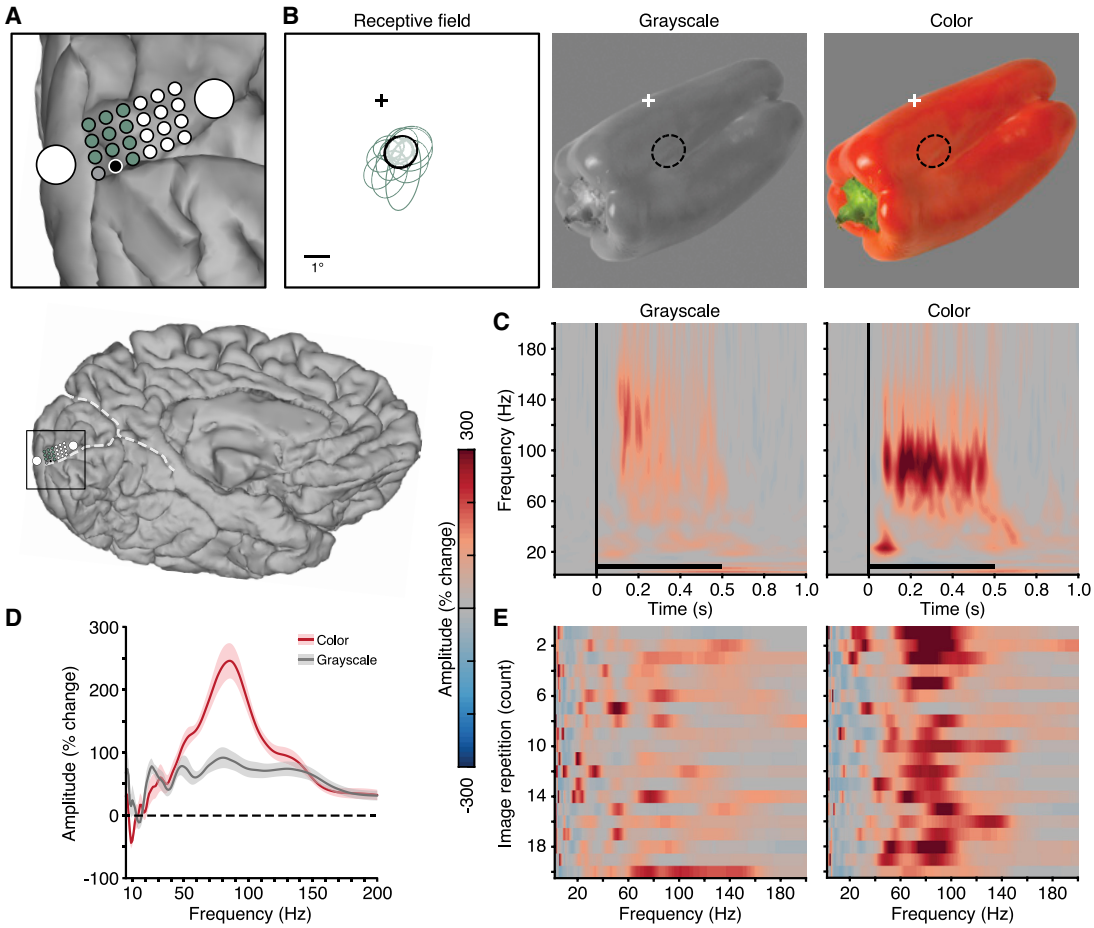

Figure 7. Experiment 4: Spectral Response Differences to Color and Grayscale Image

(A) Electrode location of macro- and mini-ECoG grid in subject N10 (whole brain location shown below for reference). Mini-ECoG electrodes with an identified receptive field are shown in green and black (gray electrode was excluded due to poor signal).

(B) Receptive fields of the 11 mini-ECoG electrodes highlighted in (A). Receptive fields are given by Gaussian fits to the data [30, 42]. The receptive field location of the black electrode in (A) is shown with respect to fixation (cross) and overlaid on both the grayscale and color images (middle and right panels; luminance values 23.8 and 24.4 cd/m^2, respectively; note: this is a cropped view of the full monitor display).

(C) Mean spectrogram response for the grayscale (left) and color (right) image versions (black electrode in A; color maps reflect % change in amplitude relative to the pre-stimulus period; black line indicates stimulus presentation).

(D) Mean normalized amplitude spectra (% change, averaged in the 250- to 500-ms post-stimulus window; shading reflects SEM) for the grayscale and color image versions.

(E) Single-trial amplitude spectra (% change, averaged in the 250- to 500-ms post-stimulus window) for each image repetition (20 repetitions; y axis) for the grayscale (left) and color (right) image versions, showing the consistency of the spectral response to repeated presentations of the same image (non-consecutive repetitions). Although the grayscale image drives a clear BBG response, the colored image drives an additional NBG peak.

activity in spectral, temporal, and functional domains. These differences have implications for functional mechanisms ascribed to NBG and BBG and more broadly to experimental design and data analysis, as discussed below.

Narrowband Gamma Activity

NBG oscillations have been proposed as a mechanism for coordinating local and distal spiking activity and supporting communication in neocortex [2]. Consistent with this view, extant evidence suggests NBG in early visual cortex influences local spiking activity [43], can synchronize with downstream targets in the visual system [44, 45], and is modulated by attention [6, 45]. Criticisms of this mechanistic view have focused on challenging the ubiquity and reliability of NBG oscillations [46]. If NBG is an important mechanism for visual perception, it should be a robust response feature that is ubiquitous across visual stimulus inputs. However, a growing literature has emphasized the strong stimulus dependence of NBG in several ways. First, NBG displays an attribute dependence, where properties of NBG, such as amplitude and frequency, are dependent on properties of the driving stimulus. This is exemplified by the data we report on the relationship between NBG peak frequency and grating contrast level (Figure 2). This grating contrast dependence was highlighted by Ray and Maunsell [21] in non-human primate V1 but has also been reported

elsewhere in human V2/3 [24] and can be detected using non-invasive methods (e.g., [26–28]).

Previous studies have also highlighted how NBG lacks reliable signal properties, such as phase stability, to support neural communication at the timescales associated with perception and cognition. For example, NBG may lack the "clock"-like attributes to synchronize distributed neural circuits [47–49], although NBG oscillations may still fulfill their functional role with variable phase and frequency attributes [50, 51]. We quantified the spatial extent of phase consistency in the NBG range, reporting evidence of a very local effect restricted to adjacent early visual locations within a few millimeters from each other (Figure 3). Although one concern is the possible influence of volume conduction on estimates of phase consistency, its influence would only suggest that our observations are overestimating the strength and spatial spread of NBG synchrony. Another aspect to consider is the different spatial pooling of intracortical and cortical surface measures, as this might complicate the comparisons with previous non-human primate findings. However, the spatial extent of phase coupling reported here was strikingly similar to those obtained with intracortical LFP recordings under similar conditions [22]. Indeed, recent evidence suggests that the LFP recorded by surface electrodes (ECoG) is relatively local [52], ensuring comparability to previous studies, especially considering the density and electrode size of our recordings.

Perhaps the most challenging finding for the role of gamma oscillations in perception is that NBG displays a class or category dependence, such that NBG responses are more reliably observed for specific types of visual stimuli. For example, NBG is highly responsive to grating-like stimuli but is often reduced or absent for more complex stimuli, such as noise patterns and natural images [46]. Earlier work in cat V1 highlighted this dependence [53], which more recently has been detailed and extended in human primary visual cortex by Hermes et al. [29] and in the present study (Figures 4 and 5). However, the principles governing this NBG stimulus dependence are subject to debate [36, 37], as some complex images may produce NBG responses [29, 35].

What factors might account for these differences? Based on our data and prior findings, two stimulus properties are critical. First, given that gratings and high-contrast edges can drive NBG oscillations, complex image stimuli may still satisfy these requirements, depending on how local image features intersect with the receptive field. Indeed, NBG responses to complex stimuli can be accurately predicted by a model built on this assumption [54]. However, this approach does not capture a second critical factor, color. For, as shown above (Figure 6), even in the absence of any spatial structure, red and orange hues are sufficient to induce NBG responses. We suggest that prior observations of NBG responses to natural images are likely to reflect the combination of receptive field size and location intersecting with local image structures and colors known to reliably drive NBG. In Experiment 4, we demonstrate how gamma responses to the same image can be dramatically modulated by image color, while keeping luminance and image structure unchanged (Figure 7). Prior work in the non-human primate previously observed larger amplitude NBG responses to certain types of color images (e.g., image of an orange) [35]. However, that finding was interpreted as being driven by the familiarity or appetitive nature of the stimulus, while our findings, and others [39], suggest a reinterpretation based on the presence of a large-field red/orange hue in the image.

Our work is the first demonstration of NBG tuning to long-wavelength hues in human visual cortex. This tuning is consistent with recent observations made in the non-human primate [39]. Importantly, another factor both influencing the amplitude of NBG response to color and its tuning across colors is the uniformity of input through the center and surround of the receptive field. Most recently, Peter et al. [40] have shown that the amplitude of NBG color responses can be further modulated by discrepancies (i.e., opponency) of color between receptive field center-surround, whereby large NBG responses to red hues are reduced by non-red colors (particularly green) occurring in the surround. This relationship can also hold for grating stimuli, depending on the uniformity of orientation through the receptive field as well as its overall size [22, 55]. In simple terms, under center-surround conditions that typically reduce firing rates, visually induced NBG is conversely enhanced [40, 56]. Multiple lines of evidence also show that NBG is reduced in amplitude or absent for stimuli that, although clearly visible, are small in size or low in contrast [40, 46, 55], adding further constraints to the stimulus dependence of NBG. By incorporating these stimulus dependencies into future models, NBG responses are likely to be well predicted across a wide range of image classes.

Broadband Gamma Activity

BBG activity takes many names in the literature, such as high gamma, "high-frequency activity," "high-frequency broadband," or "broadband" [16]. Research utilizing human intracranial recordings has particularly focused on this signal, given its many desirable properties as a marker of local neocortical response [17]. Spectrally, BBG is commonly observed as a wideband non-oscillatory signal. As shown in this study and many others, the time course of BBG is highly similar to population spiking or MUA under similar task conditions or simultaneous recording [18–20]. Despite the strong apparent temporal correlation between BBG and MUA, further work is required to elucidate the biophysical generators of this response. Clarifying these relationships may allow for improved neurophysiology interpretation of BBG and related responses, including better insight into neural population dynamics. For example, recent evidence from Leszczynski et al. [57] suggests some dissociation of BBG and MUA when considering their laminar distribution. Importantly, one practical implication of these BBG signal properties and potential generators is the uncertainty in applying "synchrony" type measures to this frequency range or interpreting power changes in BBG as changes in an oscillatory signal. Overall, although a more detailed understanding is required, the BBG signal serves as a reliable marker of electrocortical responses closely associated with population activities proximal to the electrode site [58].

Although our definition of BBG is consistent with previous studies of high-gamma activity (70–150 Hz), such ranges are often variable in the literature [16]. It is important to note that defining the band pass of BBG as 70–150 Hz is more a practical

convenience than a formal definition. As Miller et al. [17, 59] have argued, BBG is likely a wideband phenomenon that can extend into lower frequencies, overlapping with the NBG range. This overlap is clearly seen in our recordings and, as noted above, can confound analysis and interpretation of gamma amplitude or power increases as oscillatory responses. For these reasons, investigators have appropriately used more data-driven methods to model or decouple oscillatory and broadband spectral responses [29, 38, 59, 60]. Improving data-driven and physiologically informed decomposition of frequency domain analysis is therefore a critical area for development in cognitive and systems neuroscience.

Implications for Theory and Experiment

Our work highlights that NBG and BBG have distinct spectral, temporal, and functional properties, which together may help to reinterpret prior work. An intriguing example relates to past efforts to elucidate the neural correlates of blood-oxygen-level-dependent fMRI (BOLD fMRI). In a landmark paper, Logothetis et al. [61] compared electrophysiological responses (spiking, MUA, and LFP) to BOLD fMRI using a sophisticated experimental system allowing simultaneous acquisition of these data. They found that the sustained LFP signal showed the best temporal correlation with the BOLD response, unlike the more transient local MUA or single-unit spiking activity. However, these measurements were obtained from early visual cortex using checkboard stimuli, which drove sustained NBG responses. In addition, the LFP was defined as power in the 40- to 130-Hz frequency range, capturing both NBG and BBG activity [61]. It is therefore of great interest to consider how the stimulus dependence of NBG and its sustained response properties, together with the partial correlation of BBG and MUA, could provide a new interpretation of these pioneering data. In particular, the strong LFP-BOLD correlation may be less robust when using different stimulus classes and LFP frequency ranges in visual cortex. This is supported by studies inferring a close relationship between BBG, BOLD fMRI, and spiking activity [20, 62, 63]. Given the debate surrounding these relationships [64], the interpretation offered here may in part reconcile prior discrepancies.

Conclusions

Our findings integrate and extend prior work in the human and non-human primate [21, 29] and suggest that a more careful theoretical and empirical approach to gamma-range activity is required. Spectral, temporal, and functional dissociation of narrowband and broadband gamma activities suggest critical differences in these signals and warn against analyses and interpretations that may conflate them. Of particular note, the tuning of NBG to specific structural and chromatic stimulus features suggests a restricted and nuanced functional role of neocortical gamma oscillations in visual cortex. Generalizing these findings to gamma activity in other structures (e.g., hippocampus) or species should be done cautiously, as a diversity of brain circuits generate behaviorally relevant gamma-range responses [65, 66]. Indeed, although future work is required to adjudicate these more consequential mechanistic inferences, the robust stimulus-response properties of NBG may still provide a powerful methodology for studying visual circuit properties. In this sense, neocortical NBG oscillations may help us understand the mechanisms of vision without being a fundamental mechanism for vision.

STAR★METHODS

Detailed methods are provided in the online version of this paper and include the following:

- KEY RESOURCES TABLE
- LEAD CONTACT AND MATERIALS AVAILABILITY
- EXPERIMENTAL MODEL AND SUBJECT DETAILS
  - Human Subjects
- METHOD DETAILS
  - Electrode Arrays
  - Electrode Localization and selection
  - Experimental tasks
  - Experiment 1: visual grating
  - Experiment 2: visual category
  - Experiment 3: visual color
  - Experiment 4: visual color/grayscale object
  - Electrophysiological Recording
- QUANTIFICATION AND STATISTICAL ANALYSIS
  - Preprocessing
  - Spectral analysis
  - Control Analyses
- DATA AND CODE AVAILABILITY

SUPPLEMENTAL INFORMATION

Supplemental Information can be found online at https://doi.org/10.1016/j.cub.2019.08.004.

ACKNOWLEDGMENTS

We thank Ping Sun for assistance with experimental recording and Dr. Kevin Weiner for guidance on visual cytoarchitecture probability maps. This work was supported by NIH grants R01MH106700 to S.A.S., R01NS065395 to M.S.B., R01EY023336 to D.Y., and R00MH103479 and R01MH116914 to B.L.F.

AUTHOR CONTRIBUTIONS

Conceptualization and Methodology, B.L.F., W.B., M.S.B., and E.B.; Investigation and Resources, B.L.F., W.B., E.B., Y.C., S.A.S., and D.Y.; Data Curation and Software, E.B., B.L.F., and Y.L.; Writing and Visualization, B.L.F. and E.B.

DECLARATION OF INTERESTS

The authors declare no competing interests.

Received: May 15, 2019
Revised: July 1, 2019
Accepted: August 1, 2019
Published: October 3, 2019

REFERENCES

1. Fries, P. (2005). A mechanism for cognitive dynamics: neuronal communication through neuronal coherence. Trends Cogn. Sci. *9*, 474–480.
2. Fries, P. (2009). Neuronal gamma-band synchronization as a fundamental process in cortical computation. Annu. Rev. Neurosci. *32*, 209–224.
3. Singer, W. (1999). Neuronal synchrony: a versatile code for the definition of relations? Neuron *24*, 49–65, 111–125.

4. Gray, C.M. (1999). The temporal correlation hypothesis of visual feature integration: still alive and well. Neuron *24*, 31–47, 111–125.
5. Singer, W., and Gray, C.M. (1995). Visual feature integration and the temporal correlation hypothesis. Annu. Rev. Neurosci. *18*, 555–586.
6. Womelsdorf, T., Schoffelen, J.M., Oostenveld, R., Singer, W., Desimone, R., Engel, A.K., and Fries, P. (2007). Modulation of neuronal interactions through neuronal synchronization. Science *316*, 1609–1612.
7. Womelsdorf, T., Fries, P., Mitra, P.P., and Desimone, R. (2006). Gamma-band synchronization in visual cortex predicts speed of change detection. Nature *439*, 733–736.
8. Grothe, I., Neitzel, S.D., Mandon, S., and Kreiter, A.K. (2012). Switching neuronal inputs by differential modulations of gamma-band phase-coherence. J. Neurosci. *32*, 16172–16180.
9. Eckhorn, R., Bauer, R., Jordan, W., Brosch, M., Kruse, W., Munk, M., and Reitboeck, H.J. (1988). Coherent oscillations: a mechanism of feature linking in the visual cortex? Multiple electrode and correlation analyses in the cat. Biol. Cybern. *60*, 121–130.
10. Gray, C.M., and Singer, W. (1989). Stimulus-specific neuronal oscillations in orientation columns of cat visual cortex. Proc. Natl. Acad. Sci. USA *86*, 1698–1702.
11. Fries, P., Reynolds, J.H., Rorie, A.E., and Desimone, R. (2001). Modulation of oscillatory neuronal synchronization by selective visual attention. Science *291*, 1560–1563.
12. Jensen, O., Kaiser, J., and Lachaux, J.P. (2007). Human gamma-frequency oscillations associated with attention and memory. Trends Neurosci. *30*, 317–324.
13. Hall, S.D., Holliday, I.E., Hillebrand, A., Singh, K.D., Furlong, P.L., Hadjipapas, A., and Barnes, G.R. (2005). The missing link: analogous human and primate cortical gamma oscillations. Neuroimage *26*, 13–17.
14. Yuval-Greenberg, S., Tomer, O., Keren, A.S., Nelken, I., and Deouell, L.Y. (2008). Transient induced gamma-band response in EEG as a manifestation of miniature saccades. Neuron *58*, 429–441.
15. Whitham, E.M., Pope, K.J., Fitzgibbon, S.P., Lewis, T., Clark, C.R., Loveless, S., Broberg, M., Wallace, A., DeLosAngeles, D., Lillie, P., et al. (2007). Scalp electrical recording during paralysis: quantitative evidence that EEG frequencies above 20 Hz are contaminated by EMG. Clin. Neurophysiol. *118*, 1877–1888.
16. Lachaux, J.P., Axmacher, N., Mormann, F., Halgren, E., and Crone, N.E. (2012). High-frequency neural activity and human cognition: past, present and possible future of intracranial EEG research. Prog. Neurobiol. *98*, 279–301.
17. Miller, K.J., Honey, C.J., Hermes, D., Rao, R.P., denNijs, M., and Ojemann, J.G. (2014). Broadband changes in the cortical surface potential track activation of functionally diverse neuronal populations. Neuroimage *85*, 711–720.
18. Ray, S., and Maunsell, J.H. (2011). Different origins of gamma rhythm and high-gamma activity in macaque visual cortex. PLoS Biol. *9*, e1000610.
19. Manning, J.R., Jacobs, J., Fried, I., and Kahana, M.J. (2009). Broadband shifts in local field potential power spectra are correlated with single-neuron spiking in humans. J. Neurosci. *29*, 13613–13620.
20. Mukamel, R., Gelbard, H., Arieli, A., Hasson, U., Fried, I., and Malach, R. (2005). Coupling between neuronal firing, field potentials, and FMRI in human auditory cortex. Science *309*, 951–954.
21. Ray, S., and Maunsell, J.H. (2010). Differences in gamma frequencies across visual cortex restrict their possible use in computation. Neuron *67*, 885–896.
22. Jia, X., Smith, M.A., and Kohn, A. (2011). Stimulus selectivity and spatial coherence of gamma components of the local field potential. J. Neurosci. *31*, 9390–9403.
23. Berens, P., Keliris, G.A., Ecker, A.S., Logothetis, N.K., and Tolias, A.S. (2008). Comparing the feature selectivity of the gamma-band of the local field potential and the underlying spiking activity in primate visual cortex. Front. Syst. Neurosci. *2*, 2.
24. Self, M.W., Peters, J.C., Possel, J.K., Reithler, J., Goebel, R., Ris, P., Jeurissen, D., Reddy, L., Claus, S., Baayen, J.C., and Roelfsema, P.R. (2016). The effects of context and attention on spiking activity in human early visual cortex. PLoS Biol. *14*, e1002420.
25. Perry, G., Hamandi, K., Brindley, L.M., Muthukumaraswamy, S.D., and Singh, K.D. (2013). The properties of induced gamma oscillations in human visual cortex show individual variability in their dependence on stimulus size. Neuroimage *68*, 83–92.
26. Perry, G., Randle, J.M., Koelewijn, L., Routley, B.C., and Singh, K.D. (2015). Linear tuning of gamma amplitude and frequency to luminance contrast: evidence from a continuous mapping paradigm. PLoS ONE *10*, e0124798.
27. Orekhova, E.V., Sysoeva, O.V., Schneiderman, J.F., Lundström, S., Galuta, I.A., Goiaeva, D.E., Prokofyev, A.O., Riaz, B., Keeler, C., Hadjikhani, N., et al. (2018). Input-dependent modulation of MEG gamma oscillations reflects gain control in the visual cortex. Sci. Rep. *8*, 8451.
28. Hadjipapas, A., Lowet, E., Roberts, M.J., Peter, A., and De Weerd, P. (2015). Parametric variation of gamma frequency and power with luminance contrast: a comparative study of human MEG and monkey LFP and spike responses. Neuroimage *112*, 327–340.
29. Hermes, D., Miller, K.J., Wandell, B.A., and Winawer, J. (2015). Stimulus dependence of gamma oscillations in human visual cortex. Cereb. Cortex *25*, 2951–2959.
30. Yoshor, D., Bosking, W.H., Ghose, G.M., and Maunsell, J.H. (2007). Receptive fields in human visual cortex mapped with surface electrodes. Cereb. Cortex *17*, 2293–2302.
31. Fries, P., Scheeringa, R., and Oostenveld, R. (2008). Finding gamma. Neuron *58*, 303–305.
32. Cohen, A.L., Fair, D.A., Dosenbach, N.U., Miezin, F.M., Dierker, D., Van Essen, D.C., Schlaggar, B.L., and Petersen, S.E. (2008). Defining functional areas in individual human brains using resting functional connectivity MRI. Neuroimage *41*, 45–57.
33. Cohen, M.X., and Gulbinaite, R. (2014). Five methodological challenges in cognitive electrophysiology. Neuroimage *85*, 702–710.
34. Hermes, D., Miller, K.J., Noordmans, H.J., Vansteensel, M.J., and Ramsey, N.F. (2010). Automated electrocorticographic electrode localization on individually rendered brain surfaces. J. Neurosci. Methods *185*, 293–298.
35. Brunet, N., Bosman, C.A., Roberts, M., Oostenveld, R., Womelsdorf, T., De Weerd, P., and Fries, P. (2015). Visual cortical gamma-band activity during free viewing of natural images. Cereb. Cortex *25*, 918–926.
36. Brunet, N., Vinck, M., Bosman, C.A., Singer, W., and Fries, P. (2014). Gamma or no gamma, that is the question. Trends Cogn. Sci. *18*, 507–509.
37. Hermes, D., Miller, K.J., Wandell, B.A., and Winawer, J. (2015). Gamma oscillations in visual cortex: the stimulus matters. Trends Cogn. Sci. *19*, 57–58.
38. Haller, M., Donoghue, T., Peterson, E., Varma, P., Sebastian, P., Gao, R., Noto, T., Knight, R.T., Shestyuk, A., and Voytek, B. (2018). Parameterizing neural power spectra. bioRxiv. https://doi.org/10.1101/299859.
39. Shirhatti, V., and Ray, S. (2018). Long-wavelength (reddish) hues induce unusually large gamma oscillations in the primate primary visual cortex. Proc. Natl. Acad. Sci. USA *115*, 4489–4494.
40. Peter, A., Uran, C., Klon-Lipok, J., Roese, R., van Stijn, S., Barnes, W., Dowdall, J.R., Singer, W., Fries, P., and Vinck, M. (2019). Surface color and predictability determine contextual modulation of V1 firing and gamma oscillations. eLife *8*, e42101.
41. Brouwer, G.J., and Heeger, D.J. (2009). Decoding and reconstructing color from responses in human visual cortex. J. Neurosci. *29*, 13992–14003.
42. Bosking, W.H., Sun, P., Ozker, M., Pei, X., Foster, B.L., Beauchamp, M.S., and Yoshor, D. (2017). Saturation in phosphene size with increasing current levels delivered to human visual cortex. J. Neurosci. *37*, 7188–7197.
43. Womelsdorf, T., Lima, B., Vinck, M., Oostenveld, R., Singer, W., Neuenschwander, S., and Fries, P. (2012). Orientation selectivity and noise

correlation in awake monkey area V1 are modulated by the gamma cycle. Proc. Natl. Acad. Sci. USA *109*, 4302–4307.

44. Bastos, A.M., Vezoli, J., Bosman, C.A., Schoffelen, J.M., Oostenveld, R., Dowdall, J.R., De Weerd, P., Kennedy, H., and Fries, P. (2015). Visual areas exert feedforward and feedback influences through distinct frequency channels. Neuron *85*, 390–401.
45. Bosman, C.A., Schoffelen, J.M., Brunet, N., Oostenveld, R., Bastos, A.M., Womelsdorf, T., Rubehn, B., Stieglitz, T., De Weerd, P., and Fries, P. (2012). Attentional stimulus selection through selective synchronization between monkey visual areas. Neuron *75*, 875–888.
46. Ray, S., and Maunsell, J.H. (2015). Do gamma oscillations play a role in cerebral cortex? Trends Cogn. Sci. *19*, 78–85.
47. Burns, S.P., Xing, D., and Shapley, R.M. (2011). Is gamma-band activity in the local field potential of V1 cortex a "clock" or filtered noise? J. Neurosci. *31*, 9658–9664.
48. Burns, S.P., Xing, D., Shelley, M.J., and Shapley, R.M. (2010). Searching for autocoherence in the cortical network with a time-frequency analysis of the local field potential. J. Neurosci. *30*, 4033–4047.
49. Xing, D., Shen, Y., Burns, S., Yeh, C.I., Shapley, R., and Li, W. (2012). Stochastic generation of gamma-band activity in primary visual cortex of awake and anesthetized monkeys. J. Neurosci. *32*, 13873–13880a.
50. Roberts, M.J., Lowet, E., Brunet, N.M., Ter Wal, M., Tiesinga, P., Fries, P., and De Weerd, P. (2013). Robust gamma coherence between macaque V1 and V2 by dynamic frequency matching. Neuron *78*, 523–536.
51. Nikolić, D., Fries, P., and Singer, W. (2013). Gamma oscillations: precise temporal coordination without a metronome. Trends Cogn. Sci. *17*, 54–55.
52. Dubey, A., and Ray, S. (2019). Cortical electrocorticogram (ECoG) is a local signal. J. Neurosci. *39*, 4299–4311.
53. Kayser, C., Salazar, R.F., and Konig, P. (2003). Responses to natural scenes in cat V1. J. Neurophysiol. *90*, 1910–1920.
54. Hermes, D., Petridou, N., Kay, K., and Winawer, J. (2019). An image-computable model for the stimulus selectivity of gamma oscillations. bioRxiv. https://doi.org/10.1101/583567.
55. Gieselmann, M.A., and Thiele, A. (2008). Comparison of spatial integration and surround suppression characteristics in spiking activity and the local field potential in macaque V1. Eur. J. Neurosci. *28*, 447–459.
56. Vinck, M., and Bosman, C.A. (2016). More gamma more predictions: gamma-synchronization as a key mechanism for efficient integration of classical receptive field inputs with surround predictions. Front. Syst. Neurosci. *10*, 35.
57. Leszczynski, M., Barczak, A., Kajikawa, Y., Ulbert, I., Falchier, A., Tal, I., Haegens, S., Melloni, L., Knight, R., and Schroeder, C. (2019). Dissociation of broadband high-frequency activity and neuronal firing in the neocortex. bioRxiv. https://doi.org/10.1101/531368.
58. Buzsáki, G., Anastassiou, C.A., and Koch, C. (2012). The origin of extracellular fields and currents–EEG, ECoG, LFP and spikes. Nat. Rev. Neurosci. *13*, 407–420.
59. Miller, K.J., Zanos, S., Fetz, E.E., den Nijs, M., and Ojemann, J.G. (2009). Decoupling the cortical power spectrum reveals real-time representation of individual finger movements in humans. J. Neurosci. *29*, 3132–3137.
60. Winawer, J., Kay, K.N., Foster, B.L., Rauschecker, A.M., Parvizi, J., and Wandell, B.A. (2013). Asynchronous broadband signals are the principal source of the BOLD response in human visual cortex. Curr. Biol. *23*, 1145–1153.
61. Logothetis, N.K., Pauls, J., Augath, M., Trinath, T., and Oeltermann, A. (2001). Neurophysiological investigation of the basis of the fMRI signal. Nature *412*, 150–157.
62. Nir, Y., Fisch, L., Mukamel, R., Gelbard-Sagiv, H., Arieli, A., Fried, I., and Malach, R. (2007). Coupling between neuronal firing rate, gamma LFP, and BOLD fMRI is related to interneuronal correlations. Curr. Biol. *17*, 1275–1285.
63. Foster, B.L., Rangarajan, V., Shirer, W.R., and Parvizi, J. (2015). Intrinsic and task-dependent coupling of neuronal population activity in human parietal cortex. Neuron *86*, 578–590.
64. Nir, Y., Dinstein, I., Malach, R., and Heeger, D.J. (2008). BOLD and spiking activity. Nat. Neurosci. *11*, 523–524, author reply 524.
65. Cardin, J.A. (2016). Snapshots of the brain in action: local circuit operations through the lens of γ oscillations. J. Neurosci. *36*, 10496–10504.
66. Sohal, V.S. (2016). How close are we to understanding what (if anything) γ oscillations do in cortical circuits? J. Neurosci. *36*, 10489–10495.
67. Cox, R.W. (1996). AFNI: software for analysis and visualization of functional magnetic resonance neuroimages. Comput. Biomed. Res. *29*, 162–173.
68. Dale, A.M., Fischl, B., and Sereno, M.I. (1999). Cortical surface-based analysis. I. Segmentation and surface reconstruction. Neuroimage *9*, 179–194.
69. Groppe, D.M., Bickel, S., Dykstra, A.R., Wang, X., Mégevand, P., Mercier, M.R., Lado, F.A., Mehta, A.D., and Honey, C.J. (2017). iELVis: an open source MATLAB toolbox for localizing and visualizing human intracranial electrode data. J. Neurosci. Methods *281*, 40–48.
70. Brainard, D.H. (1997). The Psychophysics Toolbox. Spat. Vis. *10*, 433–436.
[71]. R Development Core Team (2010). R: A language and environment for statistical computing (R Foundation for Statistical Computing).
72. Bates, D., Maechler, M., Bolker, B., Walker, S., Christensen, R.H.B., Singmann, H., and Dai, B. (2014). lme4: Linear mixed-effects models using Eigen and S4 (Version 1.1-7). https://cran.r-project.org/web/packages/lme4/index.html.
73. Rosenke, M., Weiner, K.S., Barnett, M.A., Zilles, K., Amunts, K., Goebel, R., and Grill-Spector, K. (2018). A cross-validated cytoarchitectonic atlas of the human ventral visual stream. Neuroimage *170*, 257–270.
74. Jenkinson, M., Beckmann, C.F., Behrens, T.E., Woolrich, M.W., and Smith, S.M. (2012). Fsl. Neuroimage *62*, 782–790.
75. Henriksson, L., Nurminen, L., Hyvärinen, A., and Vanni, S. (2008). Spatial frequency tuning in human retinotopic visual areas. J. Vis. *8*, 5.1–5.13.
76. Stigliani, A., Weiner, K.S., and Grill-Spector, K. (2015). Temporal processing capacity in high-level visual cortex is domain specific. J. Neurosci. *35*, 12412–12424.
77. Brouwer, G.J., and Heeger, D.J. (2013). Categorical clustering of the neural representation of color. J. Neurosci. *33*, 15454–15465.
78. Kiani, R., Esteky, H., Mirpour, K., and Tanaka, K. (2007). Object category structure in response patterns of neuronal population in monkey inferior temporal cortex. J. Neurophysiol. *97*, 4296–4309.
79. Lachaux, J.P., Rodriguez, E., Martinerie, J., and Varela, F.J. (1999). Measuring phase synchrony in brain signals. Hum. Brain Mapp. *8*, 194–208.
80. Bartoli, E., Aron, A.R., and Tandon, N. (2018). Topography and timing of activity in right inferior frontal cortex and anterior insula for stopping movement. Hum. Brain Mapp. *39*, 189–203.
81. Shils, J.L., Litt, M., Skolnick, B.E., and Stecker, M.M. (1996). Bispectral analysis of visual interactions in humans. Electroencephalogr. Clin. Neurophysiol. *98*, 113–125.
82. Stam, C.J., Nolte, G., and Daffertshofer, A. (2007). Phase lag index: assessment of functional connectivity from multi channel EEG and MEG with diminished bias from common sources. Hum. Brain Mapp. *28*, 1178–1193.
83. Vinck, M., Oostenveld, R., van Wingerden, M., Battaglia, F., and Pennartz, C.M. (2011). An improved index of phase-synchronization for electrophysiological data in the presence of volume-conduction, noise and sample-size bias. Neuroimage *55*, 1548–1565.

STAR★METHODS

KEY RESOURCES TABLE

REAGENT or RESOURCE	SOURCE	IDENTIFIER
Software and Algorithms		
AFNI/SUMA	[67]	https://afni.nimh.nih.gov/Suma
FreeSurfer v5.3	[68]	http://freesurfer.net
iELVIS	[69]	http://ielvis.pbworks.com/w/page/116347253/FrontPage
MATLAB v2016a/v2017a/v2018a	Mathworks, MA, USA	https://matlab.mathworks.com
Psychtoolbox v3.0.12	[70]	http://psychtoolbox.org
R statistical software v3.4.3	[71]	https://www.r-project.org
LIBSVM toolbox	https://www.csie.ntu.edu.tw/~cjlin/libsvm/	https://www.csie.ntu.edu.tw/~cjlin/libsvm/
Fooof toolbox	[38]	https://github.com/fooof-tools/fooof
Lme4 library	[72]	https://stat.ethz.ch/R-manual/R-devel/library/nlme/html/lme.html
Other		
Custom Surface Electrode arrays	PMT, MN, USA	http://www.pmtcorp.com
BlackRock Cerebrus system	BlackRock Microsystems, UT, USA	https://blackrockmicro.com
vcAtlas	[73]	http://vpnl.stanford.edu/vcAtlas/
xRite i1 Pro spectrophotometer	X-Rite., MI, USA	https://www.xrite.com

LEAD CONTACT AND MATERIALS AVAILABILITY

Further information and requests for resources should be directed to and will be fulfilled by the Lead Contact, Brett L. Foster (bfoster@bcm.edu). The distribution of datasets and software used in this study is described below in the section Data and Code Availability. This study did not generate any other new material.

EXPERIMENTAL MODEL AND SUBJECT DETAILS

Human Subjects

Intracranial recordings (electrocorticography, ECoG) were obtained from 10 subjects (N1-10; 7 males, mean age 37 years, ranging from 19-54 years) undergoing invasive monitoring for the potential surgical treatment of refractory epilepsy at Baylor St. Luke's Medical Center (Houston, Texas, USA). Subject information is detailed in Table S1. All subjects provided written and verbal voluntary consent to participate in the experiments reported here. All experimental protocols were approved by the Institution Review Board at Baylor College of Medicine (IRB protocol number H-18112). We did not enroll patients with epileptic foci, anatomical abnormalities or prior surgical resection in posterior regions. No experiments were recorded in presence of inter-ictal epileptic discharges. No analyses were performed on the influence/association of sex and/or gender due to unmatched group sampling to properly evaluate such effects.

METHOD DETAILS

Electrode Arrays

All reported data were recorded using subdural cortical surface electrode strip arrays (PMT, MN, USA). Electrode arrays were custom designed to incorporate mini-ECoG electrodes (0.5 mm diameter) into a standard macro-ECoG (2 or 3 mm diameter) clinical array configuration [42]. The standard clinical ECoG strip array has 8 macro electrodes linearly arranged with a center-to-center distance of 10 mm. The mini/macro hybrid arrays used in this study had two different configurations: for hybrid array A, four mini electrodes where positioned around the first 4 macro electrodes; for hybrid array B, a high-density grid (4 × 6) of mini electrodes was positioned between the first two macro electrodes (in this configuration the distance between the first two macro electrodes was modified to be 18 mm). The two arrays are represented in Figure 1A. For subject electrode information see Table S1 and Figure S1.

Electrode Localization and selection

Electrode locations were determined by first co-registering a post-operative CT scan to a pre-operative T1 anatomical MRI scan for each subject, using FSL and AFNI [67, 74]. The cortical surface location of each electrode was based on the local projection of electrode coordinates (identified as clear hyperintensities on the aligned CT) to a cortical surface model reconstructed from the anatomical T1 scan using Freesurfer (version 5.3 [68];). Mini-ECoG electrode coordinates were often not clearly identifiable from the CT image and their position was therefore calculated with custom functions combining the macro-ECoG coordinates with the known array geometry. Electrode locations were projected onto each individual cortical surface model using AFNI/SUMA and visualized using iELVis software functions [69] in MATLAB (v2016a, MathWorks, MA, USA).

For the current study, electrodes of interest where those localized to the occipital lobe. Anatomically, the parieto-occipital sulcus served as a dorsal boundary and the lingual gyrus as a ventral boundary. Laterally, the trans-occipital sulcus and posterior aspect of the superior temporal sulcus served as dorso-lateral boundaries. Anatomical identification of occipital sites was performed with respect to each individual electrode localization. Across our sample we obtained 298 electrodes in occipital cortex (ranging from 16 to 44 within each subject). We then employed a human cytoarchitectonic atlas to evaluate the probability of each electrode to fall within one of four subdivision of visual occipital areas [73]. Atlas areas of interest for the present study were: occipital area 1, corresponding to area 17 and closely matching area V1; occipital area 2, corresponding to area 18 and closely matching area V2; occipital ventral areas 3 and 4, matching the ventral portions of V3 and V4 (see [73], for more details on area identification and cross-validation with functional subdivisions). The atlas (available at http://vpnl.stanford.edu/vcAtlas/) was mapped onto each individual cortical surface using Freesurfer (see Figure S1) such that electrodes were assigned to visual subdivisions based on locational proximity, ensuring more precision with respect to individual anatomy. The distribution of electrodes with respect to cytoarchitectonic subdivisions is reported in Table S1. As detailed below, occipital electrodes were further sub-selected by means of a functional response criterion (Figures 1B and S1). To visualize all occipital electrode locations in a common space, each electrode coordinate was transformed into the Talairach coordinate system and represented on the Colin N27 brain (Figure 1C, showing subjects N1-N7). To do so, each subject's T1 scan was transformed to match the template using AFNI, and the same transformation was applied to the electrode coordinates.

Experimental tasks

All experiments were performed at the bedside in a quiet and dimmed patient room. Subjects performed different visual tasks, detailed below (see Table S1). For all tasks, stimuli were presented on an adjustable monitor (1920x1080 resolution, 47.5x26.7 cm screen size, connected to an iMac running OSX 10.9.4) at a viewing distance of 57 cm (such that 1cm = ~1 deg visual angle). Tasks were programed using Psychtoolbox functions (v3.0.12) [70] running on MATLAB (v2017a, MathWorks, MA, USA).

Experiment 1: visual grating

In the visual grating task, subjects (N1-7) were shown full screen static grayscale grating stimuli – subtending ~25° of visual field. Grating stimuli had a sine wave spatial frequency of 1 cycle/degree to maximize V1/2 responses [75] and were presented for 500 ms with a random inter-stimulus interval (ISI) between 1500-2000 ms (see Figure 2). The timing of the stimulus presentation was selected in order to limit the influence of afterimage effects. The contrast and orientation of the stimuli were manipulated experimentally in the following way: 3 levels of Michelson contrast (20%, 50%, and 100%), and two orientations (0° and 90°). There were 30 trials for each contrast level, with equal numbers of vertical/horizontal orientation. The participants were required to maintain fixation (marked by a cross) and respond (via button press) whenever a target oddball stimulus was presented, which was a randomly occurring grating stimulus with a 45° orientation (15 targets in total, 5 for each contrast level). Performance was monitored by an experimenter present in the patient room. These target trials were not included in data analysis. Overall, the total number of trials presented was 105 with the task lasting around 6 min. The contrast levels were selected to maximize the perceptual and neural separation of stimuli and putative gamma effects, consistent with previous work [21]. Based on previous work and our own pilot studies, this range is optimal given that gratings below 20% contrast often fail to reliably produce gamma band responses [21, 24]. As grating contrast was the main manipulation of interest, all data analyses were collapsed across the two orientations (see Figure S2).

Experiment 2: visual category

In the visual category task, subjects (subjects N3-7) were presented grayscale images from 8 visual categories (faces, houses, bodies, limbs, cars, words, numbers, phase-scrambled noise) in random order (varying in position and size within a bounding box of phase-scrambled noise, subtending 15° of visual field; see Figure 4). Visual stimuli were selected from a publicly available corpus that has been successfully used as a visual category localizer in human fMRI studies [76]. Stimuli were presented for 1000 ms, with a random ISI between 1000-1500 ms. Subjects were required to respond (via button press) whenever they detected a specific stimulus being repeated back to back (1-back task). As for the first experiment, performance was monitored by an experimenter present in the patient room. The target trials were discarded from the analysis. 15 different stimuli were presented for each category and 10 random images were repeated (serving as targets), leading to a total of 130 trials. On average the task was 7 min in duration.

Experiment 3: visual color

In the visual color task, subjects (subjects N5, N8-N10) were presented full screen solid color images subtending ~25° of visual field. Colors were selected to be equally spaced, and equidistant from gray, in the *Commission Internationale de l'Eclairage* (CIE) $L^*a^*b^*$

space, within the same lightness plane ($L^* = 60$). Color selection was based on prior work in human neuroimaging [41, 77]. Descriptively, presented colors were: red, orange, yellow, green1, green2, blue1, blue2, purple and gray. During the task, subjects were required to focus on a fixation cross while static color stimuli were presented for 500 ms, with a random ISI between 1500-2000 ms (consistent with the visual grating task). Each color was presented randomly 15 times, for a total of 135 trials in each run, with the task being repeated twice (except for subject N9, who completed only one run). The participants were required to respond (via button press) whenever the target color white was presented (5 trials occurring at random in each task run). These target trials were not included in data analysis. On average the task was 5 min in duration.

Experiment 4: visual color/grayscale object

In the visual color/grayscale object task, one subject (N10) was presented images from different visual categories (20 images selected from Kiani et al. [78]) for 500 ms with a random ISI between 1000-1500 ms. Each image was repeated 20 times in random order, with the entire set of images being presented twice: first in color and then in grayscale (in separate runs, each 12 min long). The images subtended 10° of visual field and were positioned at an offset from the center of the screen based on the results of receptive field testing (Figure 7; for details on the receptive field mapping procedure see [30, 42]:). The subject was required to maintain fixation (marked by a cross at the center of the screen) and respond (via button press) whenever a target oddball stimulus was presented (an 'x' replacing the fixation cross, occurring on 18% of trials).

Electrophysiological Recording

ECoG signals were recorded at 2kHz, with a bandpass of 0.3-500Hz (4^{th} order Butterworth filter) using a 128 channel BlackRock Cerebus system (BlackRock Microsystems, UT, USA). Recordings were referenced to an inverted subdural intracranial electrode (i.e., touching the dura). Stimulus presentation was continuously logged via a photodiode sensor (attached to monitor) synchronously recorded at 30kHz. Photodiode recordings were also performed to check for any subthreshold stimulus flicker (see below).

QUANTIFICATION AND STATISTICAL ANALYSIS

Different statistical tests were employed to appropriately evaluate the effects under examination. In the following subsections, we detail analyses for signal processing, statistical testing as well as the software employed.

Preprocessing

All signal processing was performed using custom scripts in MATLAB (v2016a, MathWorks, MA, USA). Raw ECoG signals were imported into MATLAB and visually inspected for the presence of line noise, recording artifacts, and interictal epileptic spikes. Any epileptic or artifactual channel was excluded from further analysis. Each channel was notch filtered (60 Hz and harmonics) and re-referenced to the common average of all artifact-free macro-ECoG electrodes. Mini-ECoG electrodes were not included in constructing the common reference signal given that their spatial density could potentially bias the reference signal toward visual responses. Next, we employed a functional criterion to identify responsive electrodes within early visual cortex based on the presence of a visual-evoked potential (VEP). VEPs were constructed by averaging all trials (pre-processed data) for the grating task. The resulting VEP was defined as 'responsive' if it passed two criteria: 1) the standard deviation for the response window (0-250 ms, to capture the common N1/P1 response) was at least three times greater than the standard deviation for the baseline window (−1000-0 ms); 2) the voltage range for the response window was at least 10 times larger than the voltage range for baseline window. Considering all subjects, 57% of the anatomically identified occipital cortex electrodes survived this functional inclusion criterion (170 out of 298 electrodes; when considering only subjects in Experiment 1, subjects N1-N7: 133 out of 205 total electrodes, ranging from 36%–97% at the individual level) see Figure 1 and Table S1. Most of the electrodes displaying a VEP were within V1-V2 (ranging from 29% to 100% across subjects; see Table S1) with 169 out of 170 electrodes being within V1-V4 (see Figure S1). This functional criterion was employed to exclude electrodes that were not corrupted by noise but still lacked a robust signal (e.g., not making good contact on the cortex, or outside early visual areas despite anatomical selection). We used the VEP in order to limit selection bias with respect to the presence/absence of the signal of interest (i.e., the presence of narrowband or broadband gamma).

Spectral analysis

Signals from selected electrodes (i.e., continuous voltage time-series filtered and re-referenced) were downsampled to 1kHz and convolved with a family of Morlet wavelets, with central frequencies ranging linearly from 2 to 200 Hz in 1 Hz steps (7 cycles, see below for control analysis). The magnitude and angle of the complex convolution result were used as instantaneous amplitude and phase estimates as detailed below. Based on a large literature from human and non-human primate studies, narrowband gamma (NBG) was defined as neural activity between 20-60 Hz and broadband gamma (BBG) as neural activity between 70-150 Hz. The instantaneous amplitude was normalized into a percent change signal by applying a baseline correction at each time-frequency point (baseline division, using the average pre-stimulus values −500ms to 0ms for each trial). We first explored the time-frequency percent change maps averaged across trials separately for each task-specific condition (visual grating task, visual color, and visual color/grayscale tasks: time window −200 to 1000 ms around stimulus onset; visual category task: time window −200 to 1400 ms. For

all tasks, the main measures were derived from the time-frequency percent change values: the normalized amplitude spectra (obtained by averaging across the time dimension, using the 250-500 ms post-stimulus window – to avoid the transient response to stimulus onset; see Figures 2C and 2D) and the time course of NBG and BBG (obtained by averaging across the frequency dimension, using the 20-60 Hz and the 70-150 Hz ranges respectively). Additionally, power spectra for each task condition were also computed (squaring the non-normalized amplitude values for the single trial data and then averaging across time using the same windows described for the normalized amplitude spectra above). In general, all group data were first averaged across electrodes for each subject, to avoid any bias related to different number of electrodes across participants (see below for additional controls).

NBG Peak frequency

We first tested whether the frequency of NBG was modulated by the contrast level of visual grating stimuli (20%, 50%, and 100%). The single-trial normalized amplitude spectra were used to identify the frequency displaying the highest amplitude change in the narrowband gamma range (NBG, 20-60 Hz). Trials lacking a clear frequency peak were discarded (~2% of trials). The identified peak frequency and amplitude values were averaged across trials (separately for each contrast level) and across electrodes (separately for each participant). The average values (for both peak frequency and amplitude) were analyzed by means of a within-subject ANOVA, modeling the contrast levels as predictor (modeled as fixed effect, subjects as random effects) using R statistical software (v3.4.3 [71];). We performed two additional control analyses: we computed the peak frequency on the average normalized amplitude spectra (on the electrode average versus the single trials) and repeated the above ANOVA, to ensure that single-trials were able to capture the peak frequency values as reliably as the average signal with better signal to noise ratio. We also performed a mixed-effects analysis, in which we did not average across electrodes, but we modeled them as random effects. Both analyses are reported below in the Control Analyses section and are in agreement with the main analysis reported in the results section.

NBG and BBG onset latency

Next, we evaluated the onset latency of NGB oscillations. We computed the onset time of the single trial NBG amplitude change by adapting a previously published method to our data [63]. First, for each NBG signal we marked the first time point at which the NBG amplitude exceeded a threshold (> 75th percentile for at least 40 ms in the time window between −100 to 500 ms; 15% of the trials were discarded as they did not meet this criterion). Next, a 300 ms wide window was extracted around that time point (200 ms before and 100 after). This window was segmented into 50 ms bins with 20% overlap and a linear regression was fit to each bin. The first time-point of the bin with the highest slope and smallest residual error was defined as the onset of the NBG. The onset time values were averaged across trials and across electrodes and were analyzed by means of a within-subject ANOVA (as described above for the peak frequency analysis). The same procedure was repeated to estimate BBG onset latency.

Phase synchrony across trials and locations

To assess if NBG oscillations displayed phase-locking during stimulus presentation, the instantaneous phase values (the angle of the complex convolution at each time-frequency point) were used to compute two measures of phase consistency i) inter-trial phase clustering (ITPC) and inter-site phase clustering (ISPC) [33]. Specifically, the ITPC was computed at each electrode location by measuring the consistency of the instantaneous phase angle values across trials for each time-frequency point. The ISPC was computed as the across-trial consistency of the difference in phase angle values for every pair of electrodes within each subject (all combinations: n*(n-1)/2). The ISPC at each time frequency point (t,f) was calculated across trials (from tr = 1 to n) between pairs of electrodes (A and B) as:

$$ISPC_{tf} = \left| \frac{\sum_{tr=1}^{n} e^{i(\omega trA - \omega trB)}}{n} \right|$$

Where ω is the instantaneous phase angle for trial *tr* at electrode location *A* and *B*, at time *t* and frequency *f*. This measure is also known as the phase-locking statistic or value (PLV [79]; see [33] for nomenclature differences). Electrodes pairs across different arrays (subject N1) or across hemispheres (subject N3) were excluded, leading to 1252 total pairs (ranging from 36 to 465 across subjects). The raw values of both measures (ranging between 0 and 1) were baseline corrected (ranging between −1 and 1) using the average values in the pre-stimulus window (−500 to 0 ms, baseline subtraction) to allow for comparisons and averages across subjects. To perform statistical testing on the ITPC/ISPC time-frequency maps, the measures were transformed (z-fisher) at the group level (one map per subject, with 1 s pre-stimulus and 1 s post-stimulus) and permutation testing was performed to build a null distribution of values (shuffling the pre/post stimulus labels randomly across subjects 1000 times). The time-frequency ITPC/ISPC values were evaluated using an alpha level of 0.05 and subsequently a multiple comparison correction was performed by removing clusters of significance smaller than those occurring by chance ($p_{corr} < 0.05$) in the surrogate data.

Phase synchrony and inter-electrode distance

To evaluate whether ISPC occurring in the NBG range was modulated by the distance between recording sites, we modeled the relation between ISPC values and electrode distances. Specifically, the ISPC values for each electrode-pair (1252 pairs, as defined above) were averaged across time (in the 250-500 ms post-stimulus window) and across frequency (in the NBG range, 20-60 Hz). Inter-electrode distance was defined as the 'array' distance between sites (which ranged between 2 mm-8 cm). The relation between the average ISPC values and the distance (mm) between the electrodes forming each pair was modeled by fitting an exponential decay function of the form:

$$ISPC = \alpha e^{-(dist-2)/D}$$

where ISPC is the phase clustering value computed for a pair of electrodes and *dist* is the distance between that pair (in mm, note that the minimum distance between a pair of electrodes is 2 mm and this is subtracted from *dist* to re-center it on 0 mm in the equation). The coefficients α and D were estimated using nonlinear robust minimum absolute deviations fitting (statistics and machine learning toolbox in MATLAB). The coefficient α represents the initial value of ISPC at the minimal distance, while D represents the spatial decay constant, thus the distance at which the ISPC decayed to 1/*e* of its initial value. The same model (for details on starting parameters and bounds, see below) was fitted using three different measures of phase-based synchronization, yielding similar results to ISPC (magnitude squared coherence, phase-lag index and weighted phase-lag index, see Figure S6).

Visual grating contrast classification

To further test the relationship between grating contrast levels and induced NBG oscillation frequency, we sought to use NBG and BBG amplitude to classify contrast levels. We employed a support vector machine (SVM) approach using single trial spectral data from the NBG or BBG ranges to build models that would classify the three contrast levels used (20%, 50%, and 100%). The model features were vectors of amplitude values for each frequency between 20-60Hz for NBG and 70-150Hz for BBG, obtained by averaging across the 250-500ms window. These vectors of amplitude values were normalized by dividing each value by the maximum amplitude value across the frequency range. Separate models were built for NBG and BBG, with the prediction that NBG would provide higher classification accuracy given the clear changes in peak NBG frequency across contrast levels, compared with BBG. For each electrode, we used the features above to obtain classification accuracy via a leave-one-out cross validation approach. The SVM model was trained with a linear kernel and the penalty parameter set to 1. All classification analysis was performed in MATLAB (v2018a, MathWorks, MA, USA) using functions from the LIBSVM toolbox (https://www.csie.ntu.edu.tw/~cjlin/libsvm/).

Classification accuracy (for stimulus contrast) was calculated across all visually responsive electrodes, separately for NBG and BBG. To test the significance of classification values, we compared observed accuracy with a null distribution created by permutation testing (swapping trial labels prior to SVM training) 1000 times. Therefore, we obtained a classification accuracy and p value for each electrode, for both NBG and BBG. Finally, as an additional control to confirm classification was only sensitive to responses in early visual cortex, we tested all electrodes sites (beyond occipital lobe) in one subject (N7) as shown in Figure S5. As clearly shown, there was no significant classification of grating contrast levels outside of visual regions.

Power spectra parametrization and fitting

To further test for the occurrence or absence of NBG spectral peaks we adopted an alternative method to parametrize power spectra [38]. This method models power spectra as a combination of the 1/frequency component (broadband / aperiodic) in addition to a series of gaussians, which capture the presence of peaks (periodic components). The algorithm developed by Haller et al. first fits an exponential function to model the 1/f relationship (using a robust fit approach, modeling the offset, slope, and the presence of an inflexion point) and subsequently removes the fitted component, obtaining a flattened spectrum. Next, the flattened spectrum is convolved with a series of gaussians to model the presence/absence of peaks in the spectrum that were not accounted for by the aperiodic component. The presence of an oscillation or, more generally, of a peak in the spectrum will result in a successful fit of the Gaussian model, capturing the center frequency, amplitude, and bandwidth of the peak. After these steps, the full model is built based on a combination of the parameters obtained from the aperiodic fit and Gaussian fits.

We applied this method to our average power spectra values (group-level averaged, obtained by considering the 250-500 ms post stimulus window for the task data, and 200 ms pre-stimulus baseline for comparison: Figure 5). The model was fit on the frequency range between 20 and 150 Hz, by allowing the aperiodic component to have an inflexion point and by constraining the Gaussian fits to have a bandwidth between 2 and 80 Hz and to be at least 3 standard deviations above the aperiodic signal. When considering the grating task, all the contrast levels exhibited peaks with values similar to those obtained by our peak analysis in the main text (20% contrast = 31 Hz; 50% contrast = 36.5 Hz; 100% contrast = 41.2 Hz; ~9 Hz bandwidth). In opposition, the power spectra for the natural image category task resulted in model fits with no identifiable periodic components (for all categories). The aperiodic component parameters were similar across categories (offset between 11-11.6, slope between 3.6 and 3.8, inflexion point occurring between 24 and 31 Hz). The baseline power for both tasks did not exhibit any peaks and it required a slightly different model for the aperiodic component, as the inflexion point was not present. The offset and slope parameters were highly similar for the two baselines (offset: 10.6-10.7, slope 3.7 for both).

Control Analyses

Monitor and luminance testing

We performed repeated-measurements of the experimental LCD monitor using a photodiode to ensure the NBG effects reported for Experiment 1 were not confounded by sub-threshold flickering of the stimulus. The power spectrum of photodiode recordings (sampled at 30 kHz) of the stimulus monitor was computed and averaged across three repetitions of experiment 1. The mean power spectrum showed only one peak frequency at 60 Hz, matching the framerate of the LCD monitor. The 60 Hz peak in the power spectrum was not a specific feature of the presentation of the stimuli for experiment 1 (the same monitor was used to present stimuli in experiments 2, 3 and 4). In addition, as typically performed, we notched filtered intracranial recordings at 60Hz and harmonics to reduce line noise for both experiments. Therefore, we do not expect that the frame-rate of presentation (or a stimulus flicker) to be a confound on any of the effects reported. Importantly, the group mean NBG peaks we observed in Experiment 1 were 36.4 Hz, 40.2Hz, and 43.8Hz, for the 20%, 50% and 100% contrast conditions respectively (all < 60 Hz; see Figure 2).

Stimulus luminance is another critical aspect known to influence responses in early visual cortex and therefore may be driving some of the effects in our experiments. To ensure that this was not the case, for the visual color task (Experiment 3) we measured

the luminance values of each color stimulus. While color stimuli were selected from the same lightness plane (CIELAB space, L* = 60), the experimental monitor was not calibrated for equiluminance across color conditions. As differences in luminance may be a confound of the observed color differences in NBG response, we performed repeated-measurements of color luminance from the experimental monitor using an X-Rite i1 Pro spectrophotometer (X-Rite, MI, USA) controlled using MATLAB (v2016a, MathWorks, MA, USA). While luminance values varied across color stimuli (ranging between 23.6 and 40.19 cd/m^2), mean color luminance showed no correlation with the mean NBG amplitude across color conditions ($r = -0.07$, $p = 0.86$). Following a similar logic, we measured the luminance values for stimuli presented in Experiment 4, proximal to the receptive field location (Figure 7). Importantly, similar luminance values were observed for the grayscale and color images (23.8 and 24.4 cd/m^2, respectively). Therefore, the striking difference in gamma range activity between the two stimuli (Figure 7C) are unlikely to be related to such minor differences in luminance, but rather to the clear color selectivity we identify in Experiment 3 (i.e., preference for red/orange hues). In addition, comparison of the same stimulus in grayscale and color form further controls for structural differences in image statistics. Together, these results suggest our findings of differential NBG and BBG stimulus tuning are best accounted for by the spatial and color properties of presented stimuli, not their luminance.

Controls related to NBG Peak Frequency

In the main text, NBG peak frequency for a given electrode was based on identifying the peak frequency at a single-trial level (i.e., the frequency showing the maximal value of amplitude change in the NBG range, 20-60 Hz) and then averaging frequency values across trials (separately for each contrast level). The average values for each electrode were then averaged within subjects (as shown in Figure 2D) and analyzed with a within-subjects ANOVA. We performed two control analyses of the NBG peak frequency and its modulation by grating contrast level to verify that 1) consistent results would be obtained when using a different approach to identify the peak frequency (i.e., using the trial averaged amplitude change spectra) 2) a different analysis would lead to the same modulations (i.e., not averaging across trials and electrodes and including them in a mixed effects analysis).

For the first control analysis, NBG peak frequency for each electrode was estimated by identifying the frequency with maximal value of the trial-averaged normalized amplitude spectra (rather than identifying peak frequencies on single trials). We then averaged the peak frequency values within subjects and analyzed the data following the same approach as in the main text (within-subjects ANOVA). We observed highly similar results (mean peak frequency and standard error for 20% contrast: 33.4 ± 2.4 Hz; 50% contrast: 41.2 ± 2.6 Hz; 100% contrast: 44.7 ± 2.5 Hz; main contrast effect $F(2,12) = 19.2$, $p = 0.0002$; all three levels of contrast were different from each other, $p < 0.05$ Bonferroni corrected). The highly similar results confirm that the modulation of the peak frequency does not vary according to the way the peak is identified (single-trial versus trial-average), suggesting limited variability of NBG peaks across trials within electrodes.

In the second control analysis, we used the single-trial peak NBG frequencies (as in the main text) but we did not average the values across electrodes. We therefore employed a mixed effects model (using lme4 library [72] in R [71]) to evaluate the modulation of the peak NBG frequency, modeling contrast as a fixed effect and electrodes nested in subjects as random effects. The coefficients showed a similar result as reported in the main text, with a ~3 Hz shift in the peak frequency for each contrast level increment (β_0, the first fixed parameter captures the 20% contrast level mean: $\beta_0 = 36.8$ Hz, s.e. = 1.6 Hz; the other two fixed parameters capture the mean difference between 20% and 50% contrast $\beta_1 = 3.2$ Hz, s.e. = 0.3 Hz; and between 20% and 100% contrast, $\beta_2 = 6.6$ Hz, s.e. = 0.3 Hz). Additionally, to evaluate the significance of the contrast manipulation, the model was compared to a reduced model with the same random effect structure (subjects and electrodes) but no fixed effects (only an intercept term to capture the average peak frequency value, no other parameters to model the mean contrast level differences). The full model had a significantly higher goodness of fit (Akaike information criteria difference with respect to the reduced model = 370; $\chi^2(2) = 374.6$, $p < 0.0001$) demonstrating that the 2 additional parameters to model the change of peak frequency according to the contrast level significantly increased the amount of variance explained by the model. This confirms that, even when controlling for participant and electrode variation, the contrast of the grating plays a crucial role in explaining the NBG peak frequency value. Overall this analysis validates that the findings reported in the main text were not distorted by averaging across trials and electrode locations within subjects.

Controls related to NBG and BBG onset latency

To validate the reliability of the onset latency values reported in the main text, we used a different algorithm to compute the single-trial onset latency of NBG and BBG amplitude. The first order derivative of the NBG (or BBG) amplitude time series was computed and the median point between the maximum (corresponding to the highest rate of amplitude increase over time) and the neighboring zero-crossing (corresponding to the preceding local minimum) was used as an alternative onset measure [80]. This method showed a very high correlation with the method reported in the main text $r = 0.97$, $t(131) = 39.7$, $p < 0.0001$). Both methods were based on selecting the onset features of the amplitude response slope, with the metric reported here being slightly more conservative. Indeed, onset times were estimated to occur ~30 ms later with this alternative method (mean NBG onset = 157 ms, mean BBG onset = 109 ms versus values of 130 ms and 80 ms reported in the main text). Importantly, estimates were simply shifted, as the direction and magnitude of the difference between the average NBG and BBG onset times was unchanged ($t(6) = 3.8$, $p < 0.01$; mean difference ~48 ms).

Two additional controls for onset latency differences were performed to account for any influence of time-frequency decomposition parameters. First, the main text analysis was repeated on induced time-frequency data, obtained after removing the evoked components from the original voltage traces (as in Figure S3). Second, we modified the wavelet parameters used to perform the spectral decomposition and repeated the onset latency analysis (four variations: using 4, 6 or 8 cycles (fixed across frequencies) and variable cycles (from 2 to 20 cycles varying across frequencies, optimized to obtain 100 ms wavelets in the time domain, e.g., 4 cycles for a 40 Hz wavelet, etc.). The onset latency estimates for all controls were consistent with those reported in the

main text for NBG (onset values range: 128.9-141.9 ms), BBG (range: 65.7-77.6 ms) and their difference (NBG-BBG difference range: 51.6-76.2, average: 61.3 ms), validating the detection of earlier BBG onset times.

Alternative phase synchrony quantifications

In the main text, we used inter-site phase clustering (ISPC) as a measure of phase-based synchronization, to measure the consistency of the relative NBG phase position recorded at different electrode locations. Three additional measures were tested to evaluate the generalizability of the results obtained with ISPC. The first measure we tested was magnitude squared coherence [81], which differs from the ISPC as the phase similarity values are weighted by the power values (cross spectral density of the two signals, normalized by the auto-spectral density of each signal). The second measure was the phase-lag index [82], which differs from the ISPC as the clustering is considered only along the imaginary axis of the complex plane (by taking the sign of the imaginary component). This measure is less influenced by volume-conduction effects (which would have phase angle differences around 0 on the imaginary axis). The third measure was the weighted phase-lag index [83], which is a modified version of the phase-lag index that weighs more the impact of phase angle differences far from 0 on the imaginary axis, as their sign is more reliable. All measures were baseline corrected (in the same way as for the ISPC, obtaining values ranging from −1 to +1) and used as a dependent variable in the nonlinear model (described in the main text). As these measures are sensitive to different attributes of putative synchrony between two regions, they served as controls for our observed relationship between NBG ISPC and inter-electrode distance. We therefore computed the same synchrony-distance relationship for each metric, as shown in Figure S6B for the 20% contrast level.

The spatial decay constant (D) ranged between ∼2 and 4 mm depending on the measure used (20% contrast: MSC-D = 1.8 mm [95% confidence interval: 1.8:1.9]; PLI-D = 3.5 [3.4:3.7]; wPLI-D = 3.6 [3.4:3.9]; see Figure S6 for a comparison with ISPC-D: 2.3 [2.2:2.4]). The relationship between synchrony and distance did not seem to be affected by contrast (e.g., 100% contrast: MSC-D = 2.0 [1.9:2.1]; PLI-D = 2.9 [2.6:3.2]; wPLI-D = 2.7 [2.2:3.2], ISPC-D = 2.3 [2.2:2.3]), validating the reliability of the result reported in the main text across different metrics.

DATA AND CODE AVAILABILITY

All custom codes used in data pre-processing and analysis are available upon request from the Lead Contact, Brett L. Foster (bfoster@bcm.edu). Note, some codes and algorithms used in the present work are available as open source as indicated in the STAR Methods and in the Key Resources Table. All data will be uploaded to the NIMH Data Archive (NDA) following patient consent, but are available from the Lead Contact upon reasonable request.

Current Biology, Volume *29*

Supplemental Information

Functionally Distinct Gamma Range Activity Revealed by Stimulus Tuning in Human Visual Cortex

Eleonora Bartoli, William Bosking, Yvonne Chen, Ye Li, Sameer A. Sheth, Michael S. Beauchamp, Daniel Yoshor, and Brett L. Foster

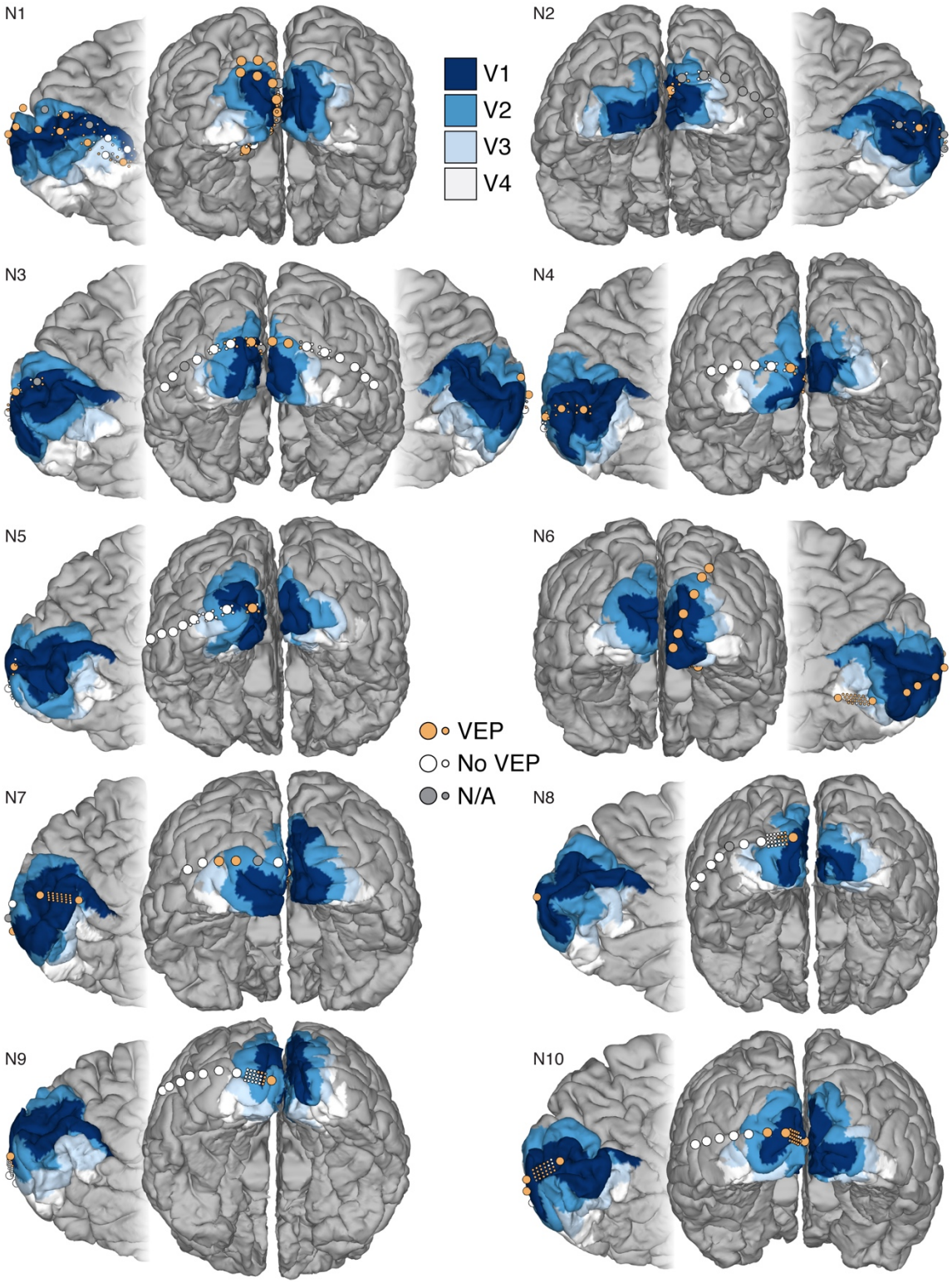

Figure S1. Single subject cortical surface and electrode array location. Related to Figure 1. Electrodes are color-coded in a similar fashion to Figure 1: orange indicates electrodes exhibiting a VEP, white indicates electrodes that did not. Additionally, gray indicates electrodes that were excluded from data analysis. The probabilistic atlas of areas V1, V2, V3 and V4 are mapped on each individual brain surface and shown as an overlay (see STAR Methods).

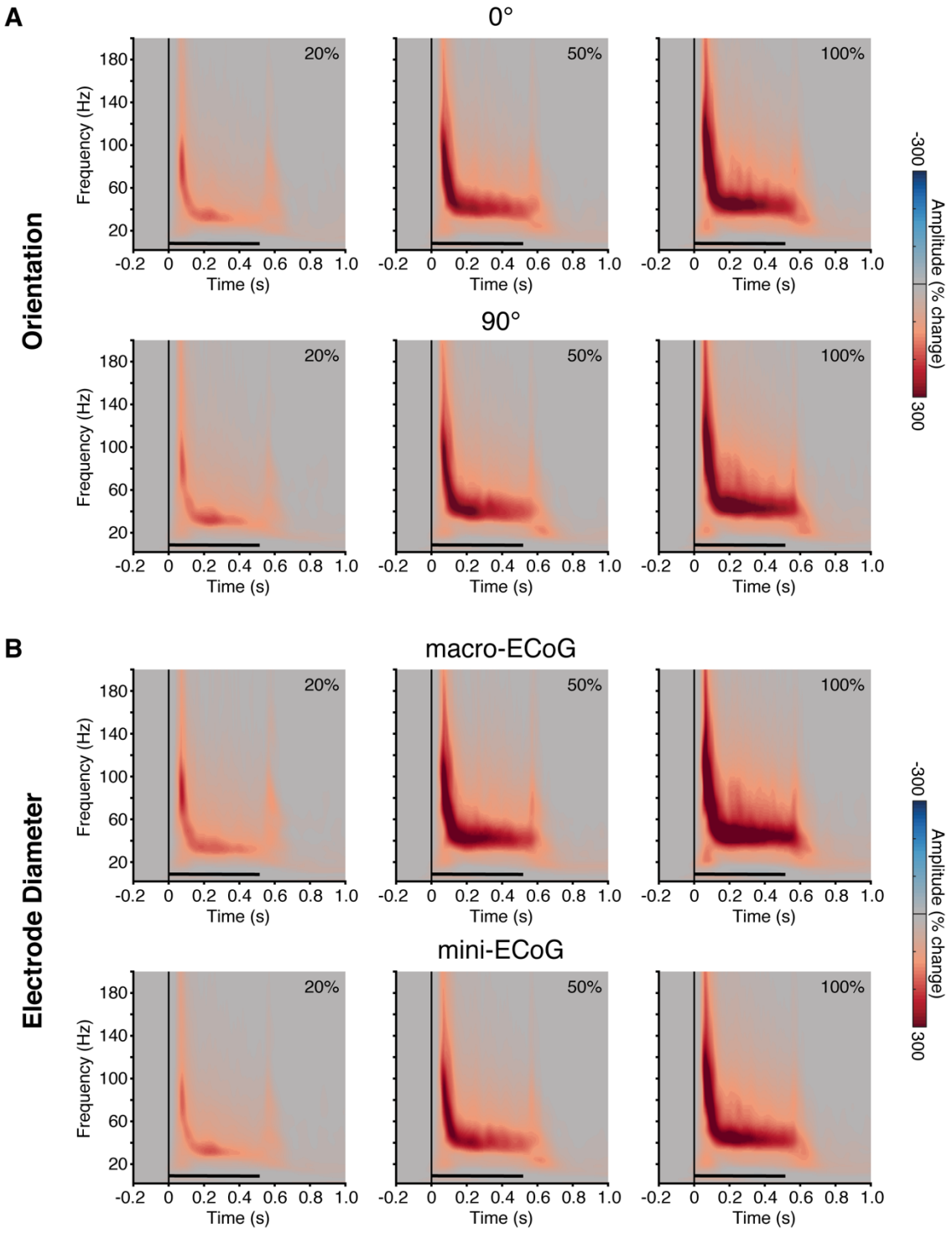

Figure S2. Influence of grating orientation and electrode size on spectral response. Related to Figure 2. Spectrograms show group average time-frequency responses for the 20%, 50% and 100% contrast levels. **A)** Spectrograms for the two grating orientations (0° and 90°). **B)** Spectrograms for the two electrode sizes (macro- and mini-ECoG). As is clear from both panels, the observed spectral responses show a striking similarity to Figure 2, supporting the combination of orientation and electrode diameter in data analyses.

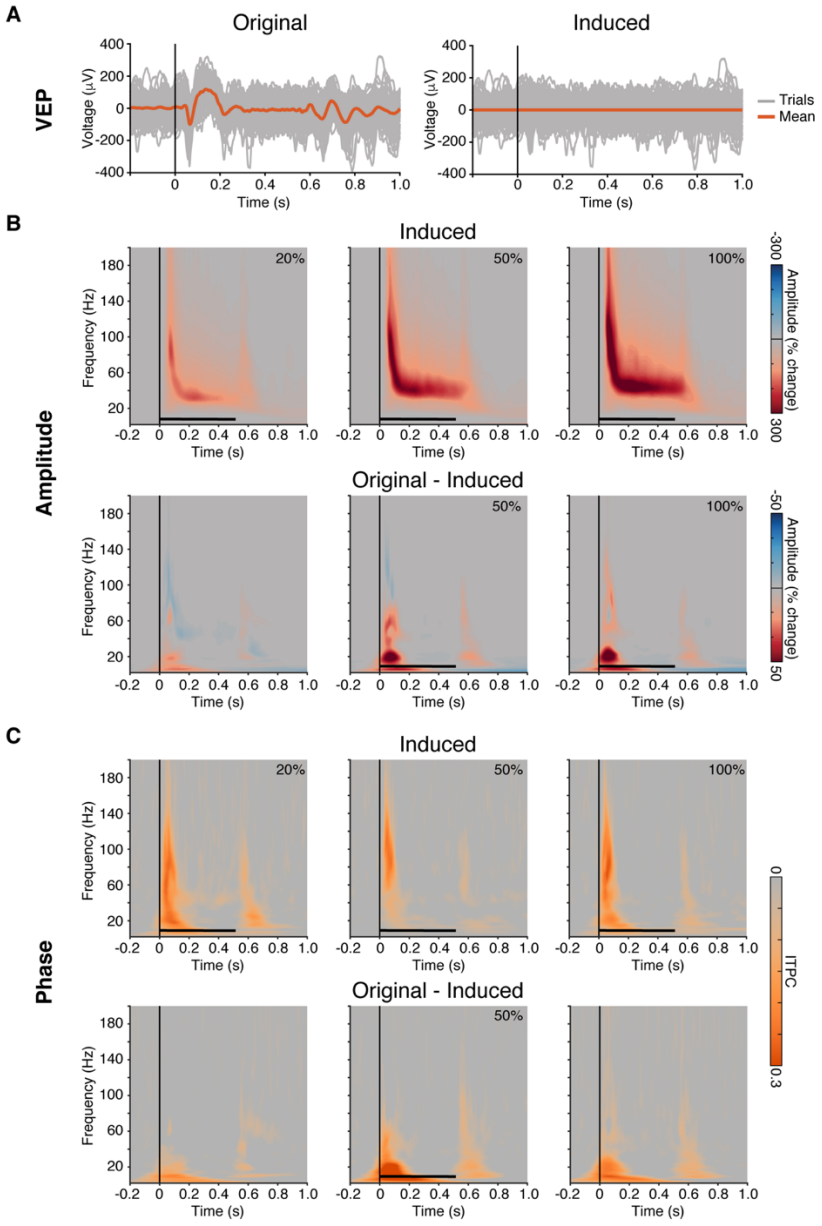

Figure S3. Influence of evoked components on spectral response. Related to Figure 2 and 3. **A)** Example of the separation between induced and evoked components: all trials recorded from one electrode (N7) are shown in gray and the average (capturing the VEP) is shown in orange (left). The average gets subtracted from each trial to obtain an induced signal (right). Spectral decomposition is then performed on the induced signal. **B)** Group mean spectrograms for the induced signal (upper) and the difference between the original signal (as reported in Figure 2) and the induced signal, reflecting the evoked components (lower). Spectrograms are for the 20%, 50% and 100% contrast levels. **C)** Same as B, for inter-trial phase clustering (ITPC). For both panels B and C, the induced spectral responses show a striking similarity to the original data reported in Figure 2 and Figure 3, respectively. These data suggest that evoked components of the VEP were not the main generators of the NBG or BBG features reported.

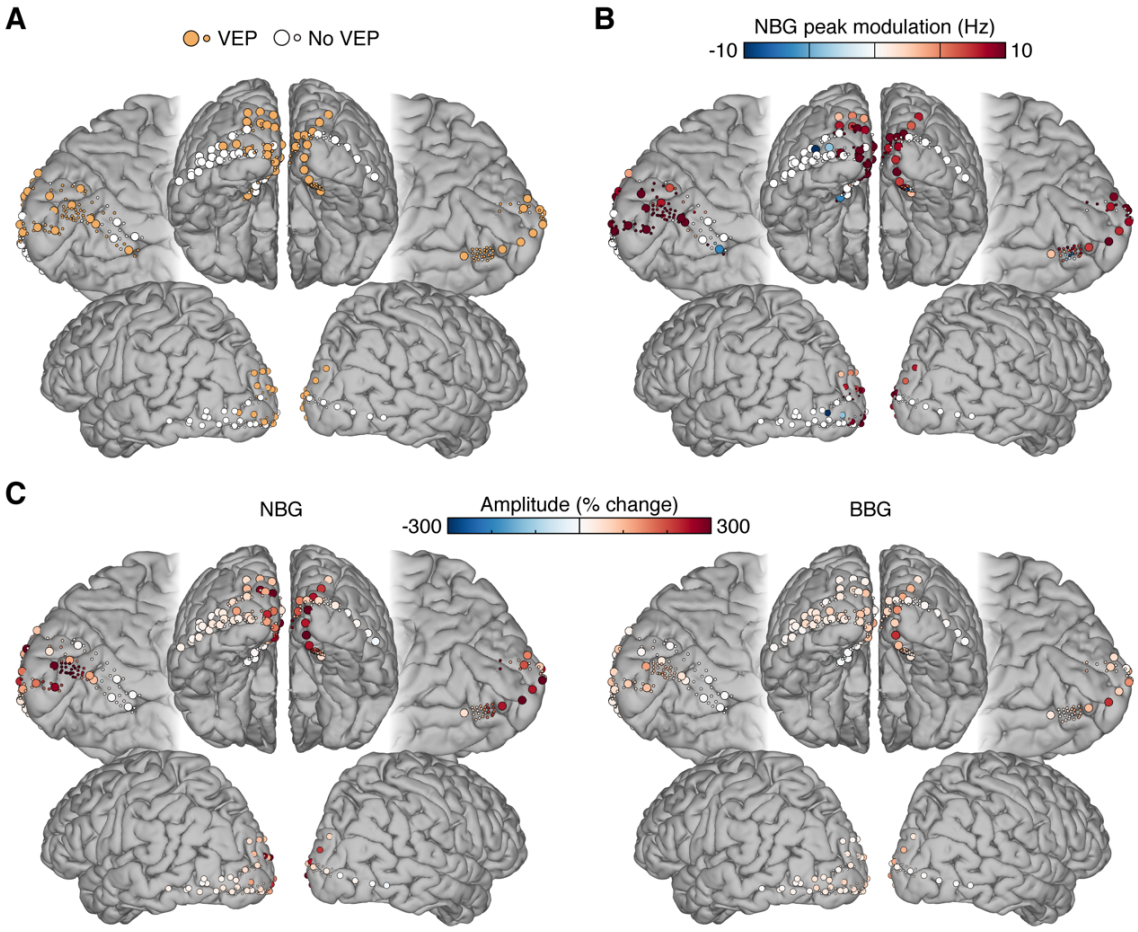

Figure S4. Influence of evoked components on the selection criterion. Related to Figure 1 and Figure 2. A) Same as Figure 1, repeated here to allow for an easier comparison with the other panels. The figure shows the occipital electrodes, colored according to the presence/absence of a visual evoked potential (VEP) which was used as a criterion to include electrodes in data analyses. As for Figure 1, the plot shows electrodes from subjects N1-N7 (as N8-10 did not perform the visual grating and object tasks). **B)** Magnitude of shift in NBG peak frequency. The contrast modulation of NBG peak frequency is represented at each electrode location (on the standard brain shown in Figure 1) and color coded according to the magnitude of frequency shift (by using the difference between the average peak frequency at 100% contrast versus 20% contrast). Note, three electrodes showed an apparent opposite modulation of the peak frequency: these electrodes did not display clear spectral increases in the lower contrast level causing a noisy estimate of the peak frequency in the NBG range. **C)** Average NBG (left) and BBG (right) amplitude (percent change in the 250-500 ms post-stimulus window) for all electrodes (VEP and non-VEP). Amplitude responses for both signals show a strikingly similar spatial distribution, being concentrated around the occipital pole, consistent with VEP data shown in A. NBG responses are higher in amplitude with respect to the BBG, confirming that the VEP criterion did not bias selection toward electrodes with larger BBG responses.

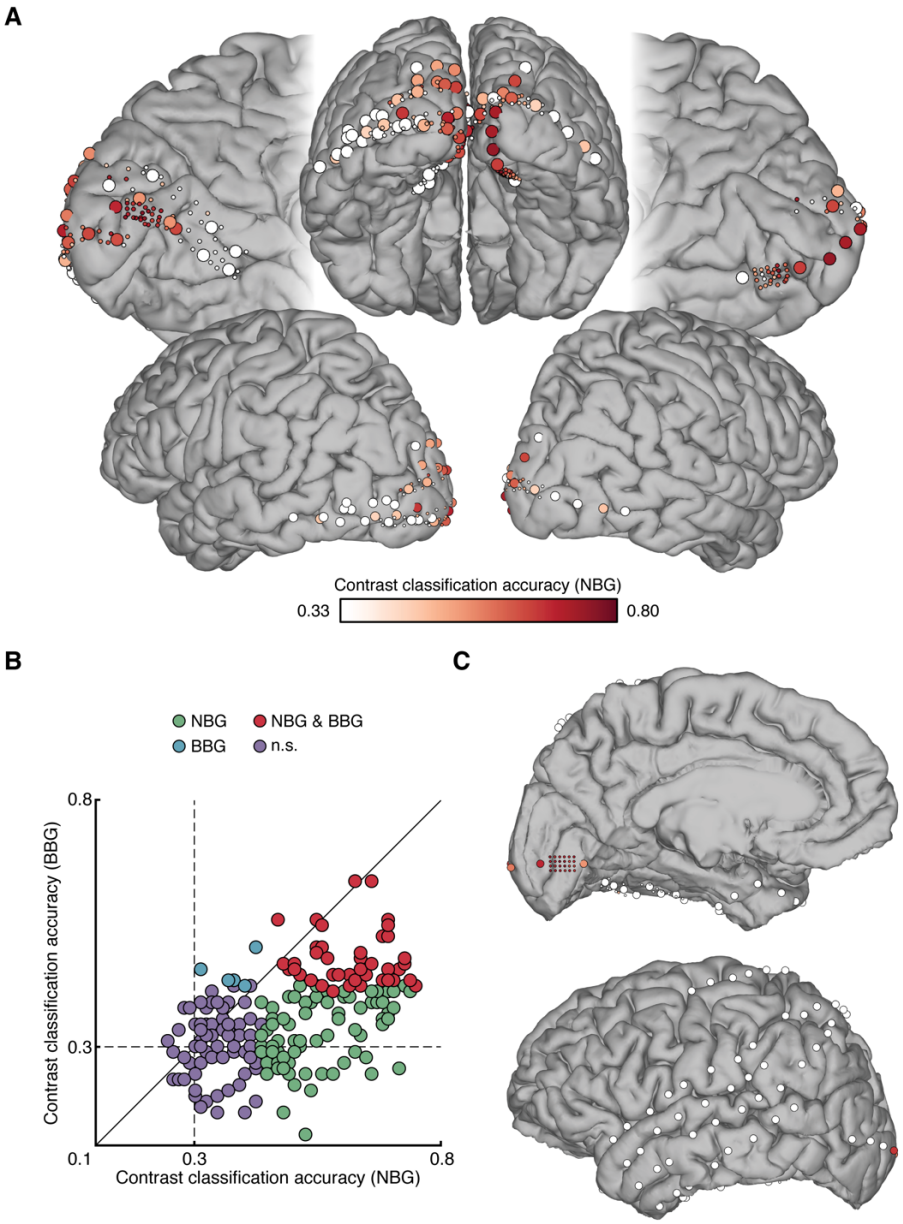

Figure S5. Classification of grating stimulus contrast. Related to Figure 1 and 2. A) Group data showing grating contrast level classification accuracy for each electrode (on the standard brain shown in Figure 1) based on a support vector machine (SVM) using averaged NBG amplitude (see Methods). Electrode locations with non-significant classification accuracy are shown in white. Note that all occipital electrodes were included in this analysis to assist in validating the VEP based selection of electrodes. There was an ~80% agreement between electrodes with above chance classification accuracy and those showing a VEP (see Figure 1 for a visual comparison). **B)** Scatter plot shows classification accuracy for the NBG-trained SVM plotted against the classification accuracy for the BBG-trained SVM for each electrode. Values are color coded according to the statistical significance of their classification accuracy (assessed with permutation testing, see Methods). **C)** Same as panel A for an individual subject (N7) showing that no electrode locations beyond the occipital lobe had above chance classification accuracy (using NBG; color map same as A).

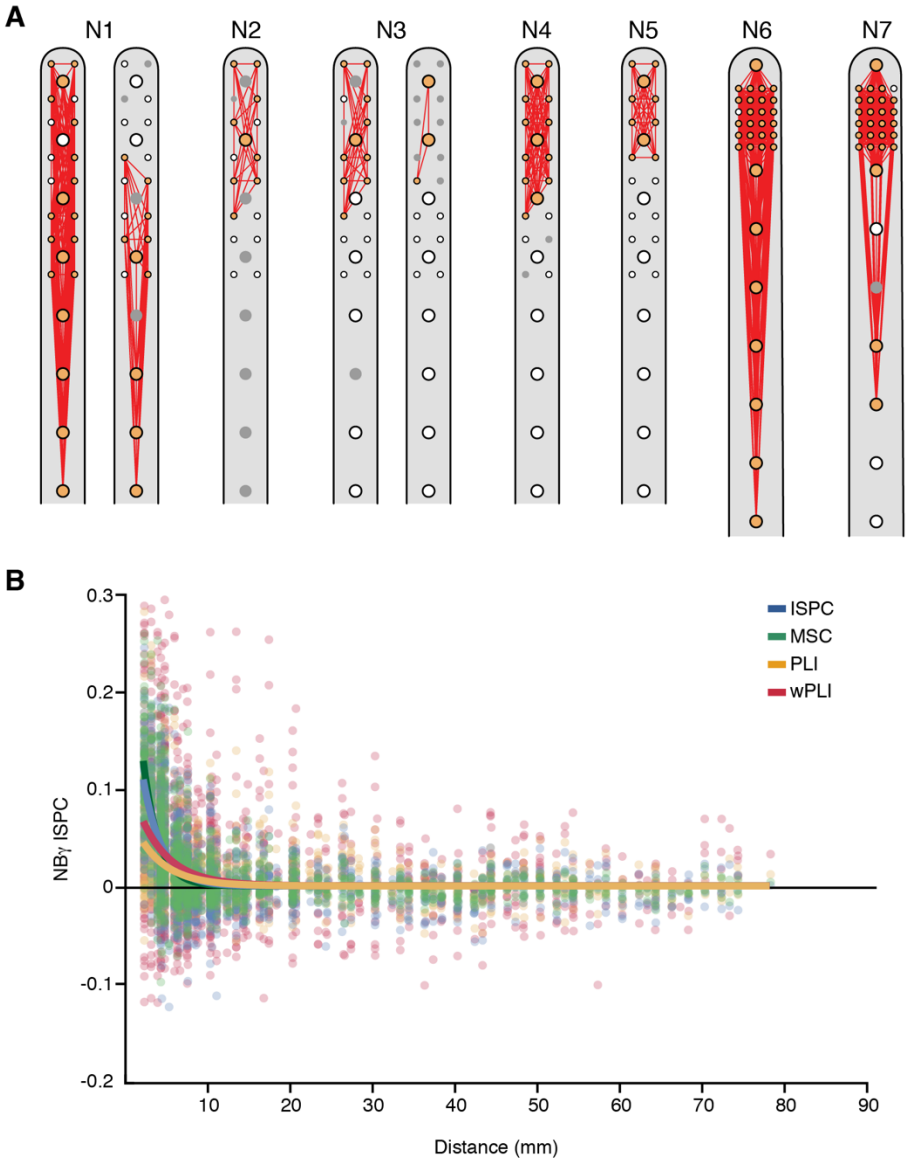

Figure S6. Electrode pairs and control metrics for NBG synchrony analysis. Related to Figure 3. A) Electrode array configurations for all subjects (N1-7), where red lines indicate all electrode pairs used in the phase-based synchrony analyses (electrode colors same as Figure S1). **B)** Scatter plot shows a comparison between the decay of NBG phase based synchrony over inter-electrode distance using different metrics (ISPC, inter-site phase clustering, MSC: mean squared coherence, PLI: phase lag index and wPLI: weighted phase lag index; see STAR Methods). Data is shown for the 20% contrast condition.

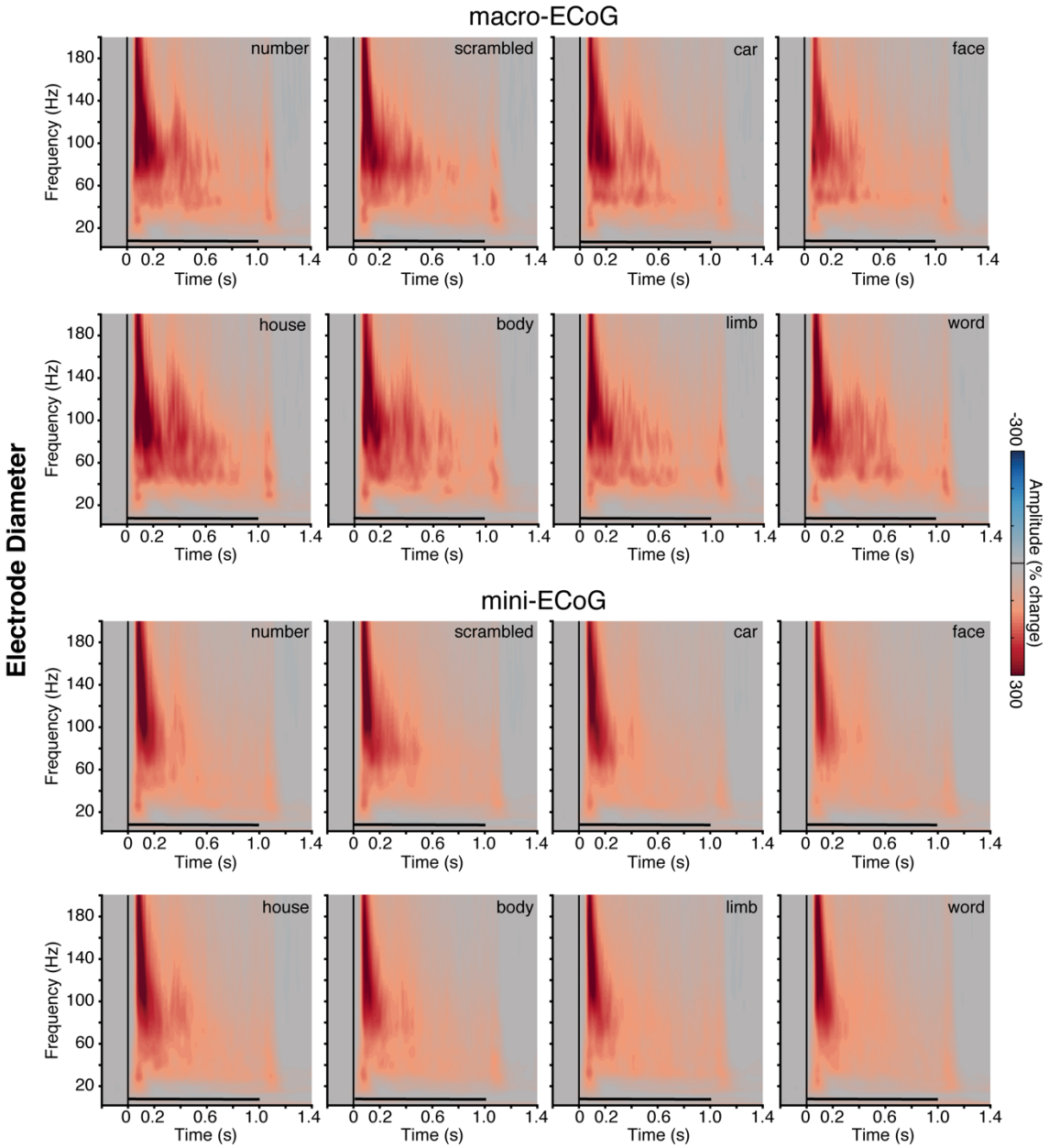

Figure S7. Influence of electrode size on spectral response in Experiment 2. Related to Figure 4. Spectrograms show group average time-frequency responses for the natural image categories in experiment 2. Spectrograms for the two electrode sizes (macro- and mini-ECoG) display similar responses to those reported in Figure 4, where electrode size was collapsed in data analyses. Macro-ECoG responses show some qualitative differences, with a longer duration BBG response, however they remain highly distinct from responses observed for Experiment 1.

# Subj	Sex	Age	Exp	Elec Array Configuration		# Elecs in OC						% OC Elecs in V1/V2		# Elecs with VEP in OC						% VEP Elecs in V1/V2	
				LH	RH	TOT	V1	V2	V3	V4	N/A	In V1/ V2	Out V1/V2	TOT	V1	V2	V3	V4	N/A	In V1/ V2	Out V1/V2
1	M	32	1	Ax2	-	44	20	12	9	3	-	73	27	29	15	9	3	2	-	83	17
2	M	44	1	-	A	16	10	5	1	-	-	94	6	9	8	1	-	-	-	100	-
3	M	54	1-2	A	A	36	10	6	4	-	16	44	56	13	9	3	1	-	-	92	8
4	M	20	1-2	A	-	22	11	6	1	1	3	77	23	14	11	3	-	-	-	100	-
5	M	47	1-2-3	A	-	24	5	6	6	3	4	46	54	10	5	5	-	-	-	100	-
6	F	37	1-2	-	B	32	3	6	15	7	1	28	72	31	3	6	14	7	1	29	71
7	M	25	1-2	B	-	31	26	3	1	-	1	94	6	27	25	2	-	-	-	100	-
8	M	53	3	B	-	31	1	15	1	-	14	52	48	8	1	7	-	-	-	100	-
9	F	19	3	B	-	31	6	18	1	-	6	77	23	6	2	4	-	-	-	100	-
10	F	41	3-4	B	-	31	25	2	1	-	3	87	13	23	22	1	-	-	-	100	-
						298	117	79	40	14	48			**170**	101	41	18	9	1		

Table S1. Subject and Electrode Information. Related to STAR Methods: Experimental Model and Subject Details. For each subject (#Subj 1-10, in bold) demographic and experimental information is reported in the following order: Sex (Male/Female), Age at time of experiment (years), the Experiments that were performed (Exp 1 = visual grating task, 2 = visual category task, 3 = visual color task, 4 = visual color/grayscale object task), Electrode Array Configuration (A or B) and the hemisphere on which it was placed (Left/Right). The electrode count in the region of interest (#Elecs in Occipital Cortex; OC) is subdivided by the total count (TOT) and the count within visual regions (V1,V2,V3,V4, see STAR Methods) and those not assigned to those regions (N/A). The percentage of occipital electrodes in V1/V2 (% OC Elecs in V1/V2) versus the percentage of electrodes outside V1/V2 (with respect to the total count) is reported. Lastly, the electrode count in occipital cortex of electrodes displaying a visual evoked potential (VEP, i.e. the electrodes that were used in all analyses, unless otherwise specified) is reported. The total count is subdivided by each visual region (V1, V2, V3, V4 & not assigned) as well as the percentage of VEP electrodes within and outside of V1/V2.